LA-UR-08-07774

Approved for public release;
distribution is unlimited.

Title:	Modeling metallic single crystal plastic hardening through the evolution of dislocation subgrain structures
Author(s):	Benjamin L Hansen
Intended for:	PhD Thesis at California Institute of Technology

Modeling Metallic Single Crystal Plastic Hardening through the Evolution of Dislocation Subgrain Structures

Thesis by

Benjamin L. Hansen

In Partial Fulfillment of the Requirements

for the Degree of

Doctor of Philosophy

California Institute of Technology

Pasadena, California

2009

(Defended January 13, 2009)

Dedicated to those who inspire and those I relied on through the mire of discovering insight.

Acknowledgments

I would like to acknowledge the support of the Accelerated Strategic Computing Initiative (ASCI) both at the California Institute of Technology and at Los Alamos National Laboratory in funding this work.

Abstract

A single crystal plasticity theory for insertion into finite element simulation is formulated using sequential laminates to model subgrain dislocation structures. It is known that local models do not adequately account for latent hardening, as latent hardening is not only a material property, but a nonlocal property (e.g., grain size and shape). The addition of the nonlocal energy from the formation of subgrain structure dislocation walls and the boundary layer misfits provide both latent and self hardening of crystal slip. Latent hardening occurs as the formation of new dislocation walls limit motion of new mobile dislocations, thus hardening future slip systems. Self hardening is accomplished by evolution of the subgrain structure length scale. No multiple slip hardening terms are included.

The substructure length scale is computed by minimizing the nonlocal energy. The minimization of the nonlocal energy is a competition between the dislocation wall and boundary layer energy. The nonlocal terms are also directly minimized within the subgrain model as they impact deformation response. The geometrical relationship between the dislocation walls and slip planes affecting dislocation mean free path is accounted for giving a first-order approximation to shape effects. A coplanar slip model is developed due to requirements when modeling the subgrain structure. This subgrain structure plasticity model is noteworthy as all material parameters are experimentally determined rather than fit. The model also has

an inherit path dependency due to the formation of the subgrain structures. Validation is accomplished by comparison to single crystal tension test results.

Contents

List of Figures

List of Tables

Chapter 1

Introduction

Previous work investigating microstructures and plasticity have uncovered that if a single crystal deformed by plastic slip has latent hardening and is allowed to form arbitrarily fine subgrain microstructure without any energy penalty for the accumulation of dislocations, then each slip system will appear macroscopically to harden independently [1]. This occurs because the microstructure forms in such a way to limit interaction between slip systems. This observation is in conflict with experimental data demonstrating that two active slip systems exhibit latent hardening [2]. As research also indicates that latent hardening is not a material property, but rather depends on the crystal grain in which the material deforms (e.g., grain shape and size); it is realized that the observed latent hardening is a property of interactions due to the microstructure. This work attempts to add microstructure hardening interactions into a constitutive crystal plasticity code for use as a material model in finite element calculations.

Figures 1.1 and 1.2 display the formation of typical subgrain structures in two different copper specimens taken using a transmission electron microscope. The images are courtesy of Cerreta [3]. Figure 1.1 is a cell structure frequently seen during initial plastic deformation. The walls between the cells are formed by the accumulation of random dislocations that cause a very low angle misorientation. These are frequently referred to as incidental dislocation

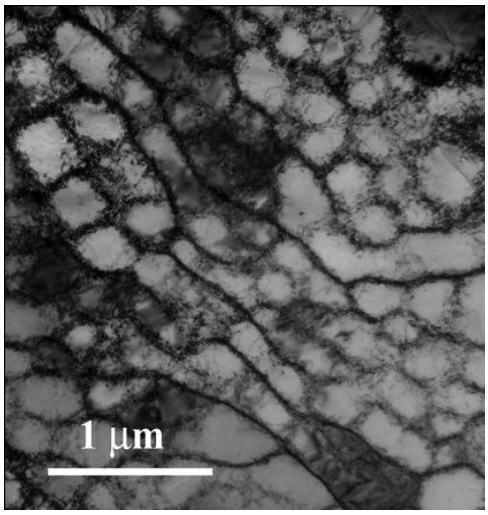

Figure 1.1. *Classic subgrain cell structure in high-purity copper (Cerreta [3]).*

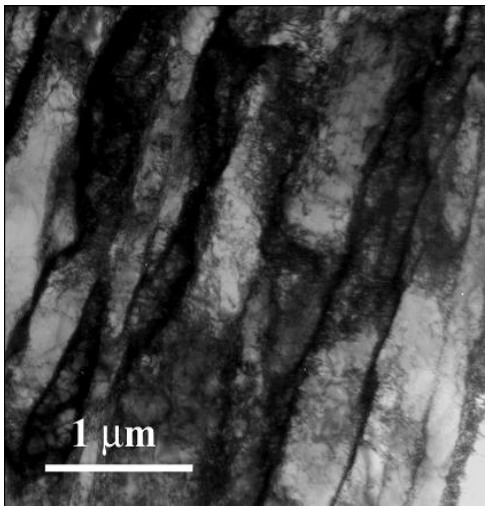

Figure 1.2. *Laminate subgrain structure formed by elongation of cell walls in copper (Cerreta [3]).*

boundaries (IDB). Upon further deformation, the cell walls tend to elongate and increase in misorientation angle to form parallel dislocation walls similar to a laminate structures as seen in figure 1.2. The formation of the elongated walls is associated with a strain difference between the sides. These are called geometrically necessary boundaries (GNB). For a full review of deformation laminate microstructures the reader is referred to the works of Hansen and Hughes [4, 5, 6]. These works include an analysis of the subgrain microstructures on which this model is based as well as scaling laws for the structures. The work of Ortiz and Repetto [7] also contains a comparison between the laminate microstructure model used in this work and many experimentally observed subgrain structures. Steeds [8] provides a study of single crystal copper dislocation structures as a function of strain.

Initial investigations into modeling subgrain microstructure development and plastic deformation were conducted by Repetto and Ortiz [7]. Their work derived the property that in order to minimize energy, subgrain microstructures should form regions of single slip. They also compared microstructure configuration compatibility to commonly observed experimental microstructures and found good agreement.

The work of Ortiz, Repetto, and Stainier [9] followed in which the ideas of Repetto and Ortiz were implemented into a finite deformation constitutive model that explicitly resolved laminate microstructures. It demonstrated the possibility of capturing grain size effects on deformation and contains the first implementation of nonlocal energy into the laminar microstructures. Comparisons are made between the direct simulation of subgrain dislocation microstructures to obtain size effects and the nature of size effects obtained by the strain gradient method.

The previous work was built upon by Aubrey and Ortiz [10], in which the model was streamlined for easier energy calculations and infinite latent hardening. Aubrey and Ortiz

compared the scaling of the formed microstructures to the scaling law of Hughes et al. [5]. Much of this current work follows directly from the ideas of Aubrey and Ortiz, but varies greatly in the implementation of those ideas. This work also compares more directly to experimental measurements.

At this point, the theory of laminate microstrcutures has diverged onto several distinct paths. The work of Aubrey, Fago, and Ortiz [11] considered the relaxation of martensitic materials using subgrain microstructure with branching and pruning operations. The work of Conti, Hauret, and Ortiz [12] considered the application of minimization principles directly rather than explicitly resolving the microstructure, such that calculations can determine stress states and the microstructures can be resolved after calculations are complete. This is being further explored by Gurses [13]. The work of Conti and Ortiz [1] considered linearized kinematics and the formation of microstructures. Conti and Theil [14] considered single-slip finite deformation microstructures in which elastic structures are permitted.

An understanding of traditional plasticity theories is useful for understanding this work, as many sound principles from those works are used. A selection of models includes Cuitino and Oritz [15] and Bronkhorst et al. [16]. It should be emphasized that these are local models which contain latent hardening in multiple slip, but do not attempt to model microstructure and nonlocal energy.

In this work, the model introduced by Ortiz, Repetto, and Stainier [7, 9] and investigated by Aubrey and Ortiz [10] is further developed. Differences and extensions of the current methodology are highlighted. The new developments in this work include the evolution of the subgrain microstructure lengths to treat hardening behavior, a method that accounts for unique features of coplanar slip systems, effects of grain shape and microstructure wall normal orientation on the mean free path of dislocations, direct incorporation of the nonlocal

energy in the minimization of deformation energy (rather than as a perturbation), corrections to the boundary layer energy formulation, and an investigation of the subgrain laminate wall normal implementation. The discontinuities that develop in the stress and material tangents when microstructures form are also discussed to allow for use of traction boundary conditions.

In chapter 2, the general constitutive framework of a single crystal incorporating both elastic and plastic deformation is presented. Coplanar slip is developed separately. The general framework is then applied to laminate microstructures which include nonlocal energy terms in chapter 3. The nonlocal energy terms are derived after the laminate microstructures as this gives the presentation a more concise flow, although the reader needs to accept the nonlocal terms before they are developed. This order prevents the presentation of the model initially without nonlocal terms and then a second time with the nonlocal terms included. The equilibration of the microstructure for new deformation states is described afterward. Significant changes have been added to the nonlocal energy and equilibration. Chapter 3 also includes how stress state discontinuities that arise when a new microstructure forms are treated numerically. Last, the model is validated by simulating experimental tests of copper single crystals (chapter 4). Comparisons are made with variations in single crystal stress response due to crystal orientation, grain size, and grain shape. The subgrain structures are also compared to traditional single crystal plasticity theories. Conclusions are drawn and future work is presented in chapter 5.

Chapter 2

Material Model

The model is concerned with determining the reaction of a crystalline material occupying a volume Ω when a deformation mapping $y[\mathbf{x}] : \Omega \rightarrow R^3$ is applied. The deformation gradient is defined by

$$\mathbf{F}[\mathbf{x}] \equiv \nabla y[\mathbf{x}] \quad , \tag{2.1}$$

where ∇ is the gradient operator. The brackets [.] are used to display a dependence in this work, whereas (.) are used to show order of operations or to distinguish superscripts from exponents.

In anticipation of applying the model at a material integration point within a continuum scale application any dependence on the position variable $\mathbf{x}$ will be dropped. Thus, all equations apply for a given value of $\mathbf{x}$, e.g., $\mathbf{F}[\mathbf{x}] \rightarrow \mathbf{F}$. The value $\mathbf{F}$ will be referenced as the "global" or "macroscopic" deformation. The microstructure at the material point $\mathbf{x}$ is being simulated.

Indices will be used frequently in notation. To keep the meaning of indices clear, they will always be placed in identical positions. The upper right will be used for modifying quantities, such as differentiating between plastic and elastic values; the lower left for discretization or

iteration; and the lower right for other enumeration, such as over slip systems or laminate structures.

$$_{discretization}X^{modifier}_{enumeration}$$

2.1 Constitutive Framework

First, a Helmholtz free energy density $\phi[\mathbf{F}, \mathbf{q}]$ per undeformed unit of volume which depends upon the deformation gradient $\mathbf{F}$ and a set of internal state variables $\mathbf{q}$ is considered. No temperature or strain rate dependence is taken into account in this work. When no viscosity is present, Coleman's relations give the First Piola-Kirchoff stress tensor, $\mathbf{P}$, as

$$\mathbf{P} = \frac{\partial \phi[\mathbf{F}, \mathbf{q}]}{\partial \mathbf{F}} \quad . \tag{2.2}$$

The material tangent is defined by

$$\mathcal{C} \equiv \frac{\partial \mathbf{P}}{\partial \mathbf{F}} \quad . \tag{2.3}$$

This is required by the iterative solvers of the finite element method. The general material formulation for the tangents can be found in Ortiz and Stainier [17].

Following Rice [18], an inelastic potential, ψ, is also introduced along with the corresponding thermodynamic force, $\mathbf{Q}$, conjugate to the internal variables $\mathbf{q}$

$$\mathbf{Q} = -\frac{\partial \phi[\mathbf{F}, \mathbf{q}]}{\partial \mathbf{q}} \quad , \tag{2.4}$$

$$\dot{\mathbf{q}} = \frac{\partial \psi[\mathbf{Q}, \mathbf{q}]}{\partial \mathbf{Q}} \quad , \tag{2.5}$$

where a " ˙ " indicates time derivative. All these relations are subject to material frame indifference, see references [9, 17] for consequences.

2.2 Single Crystal Model

The proceeding framework is now applied to a single crystal. The full deformation of a material point is composed of multiple deformation gradients, an elastic, followed by multiple plastic.

A multiplicative decomposition of the deformation gradient proposed by Lee [19] is adopted

$$\mathbf{F} = \mathbf{F}^e\mathbf{F}^p \quad , \tag{2.6}$$

where $\mathbf{F}^e$ is an elastic deformation which distorts the crystalline lattice and $\mathbf{F}^p$ is the total plastic deformation caused by dislocation motion. The plastic deformation is assumed to leave the crystal lattice undistorted, at least at the macroscopic continuum level.

For metallic crystals, it is also reasonable to assume the energy can be split into an elastic portion, W^e; and a plastic, dislocation stored energy, W^p.

$$\phi = W^e[\mathbf{F}^e] + W^p[\mathbf{F}^p, \gamma_\alpha] \quad , \tag{2.7}$$

with W^p being a function only of the plastic internal variables, specifically, the slip system strains, γ_α, and $\mathbf{F}^p$. Application of (2.2) gives

$$\mathbf{P} = \frac{\partial W^e[\mathbf{F}^e]}{\partial \mathbf{F}^e}(\mathbf{F}^p)^{-T} \quad . \tag{2.8}$$

The stress tensor

$$\mathbf{P}^e \equiv \mathbf{P}(\mathbf{F}^p)^T \tag{2.9}$$

is defined for later use.

Following the formulation of Ortiz and Repetto [7] the forces conjugate to the internal variables $\mathbf{F}^p$ and γ yields

$$\mathbf{S} \equiv -\frac{\partial \phi}{\partial \mathbf{F}^p} = (\mathbf{F}^e)^T \frac{\partial W^e}{\partial \mathbf{F}^e} (\mathbf{F}^p)^{-T} \quad , \tag{2.10}$$

which is obviously related to the symmetric second Piola-Kirchoff stress tensor, and,

$$g \equiv \frac{\partial \phi}{\partial \gamma} \quad , \tag{2.11}$$

with accompanying flow and hardening rules from (2.5)

$$\dot{\mathbf{F}}^p = \frac{\partial \psi}{\partial \mathbf{S}} \quad , \tag{2.12}$$

$$\dot{\gamma} = -\frac{\partial \psi}{\partial g} \quad . \tag{2.13}$$

Note, $\dot{\gamma}_\alpha$ is the rate of slip strain on slip system α.

2.2.1 Elastic Deformation Model

For the elastic portion of the deformation, a Saint Venant-Kirchoff material is used. It is defined by the following equations. Starting with the Green-Lagrange Strain Tensor

$$\mathbf{E}^e = \frac{1}{2}((\mathbf{F}^e)^T \mathbf{F}^e - \mathbf{I}) \quad , \tag{2.14}$$

where $\mathbf{I}$ is the identity tensor. The second Piola-Kirchoff stress tensor follows by assuming a linear relationship with the crystal's elasticity constants, $\mathcal{C}^{mat}$,

$$\mathbf{K}^e = \mathcal{C}^{mat} \cdot \mathbf{E}^e \quad . \tag{2.15}$$

An assumption of linearity here is generally sufficient for the elastic portion of deformation for metallic materials [15]. Higher-order moduli are available in Teodosiu [20]. The First Piola-Kirchoff stress tensor for an elastic deformation follows as

$$\mathbf{P}^e = \mathbf{F}^e \mathbf{K}^e \quad . \tag{2.16}$$

One needs to note that $\mathbf{P}^e$ relates to the overall $\mathbf{P}$ by use of equation (2.9)

The elastic energy density is computed

$$W^e = \frac{1}{2} \mathbf{K}^e \cdot \mathbf{E}^e \quad . \tag{2.17}$$

The material tangent for elastic deformation is given by indicial notation for ease.

$$\mathcal{C}^e_{iJkL} = \frac{\partial \mathbf{P}^e}{\partial \mathbf{F}^e} = \delta_{ik} K^e_{JL} + 2 F^e_{iM} F^e_{kN} \mathcal{C}^{mat}_{MJNL} \quad , \tag{2.18}$$

where δ_{ab} is the Dirac operator defined by

$$\delta_{ab} = \begin{cases} 1 & \textit{if } a = b, \\ 0 & \textit{otherwise} \end{cases} \quad .$$

2.2.2 Plastic Deformation Model

The shear stress acting on slip system α is resolved geometrically as

$$\tau_\alpha = \mathbf{P}(\mathbf{F}^p)^T \cdot (\mathbf{F}^e \mathbf{s}_\alpha \otimes \mathbf{m}_\alpha) = \mathbf{S}(\mathbf{F}^p)^T \cdot (\mathbf{s}_\alpha \otimes \mathbf{m}_\alpha) \quad ; \tag{2.19}$$

where the $\cdot$ operator between two higher-order tensors is defined as $A \cdot M = A_{..kl} M_{kl..}$, using Einsteinian notation to indicate the indices k and l are summed over; $\mathbf{m}_\alpha$ is the slip plane normal; and $\mathbf{s}_\alpha$ is the slip direction of system α. Again following Rice [18], the flow rule is given a potential structure by assuming the potential of each slip system can be summed

$$\psi(\mathbf{S}, g; \mathbf{F}^p, \gamma) = \sum_{\alpha=1}^{N} \psi_\alpha(\mathbf{S}, g_\alpha; \mathbf{F}^p, \gamma_\alpha) \quad . \tag{2.20}$$

An application of Schmidt's Rule: $\psi_\alpha = \psi_\alpha(\tau_\alpha - g_\alpha)$, demonstrates that g is the critical resolved shear stress, τ_α^c, or stress at which slip system α activates.

The flow rule for plastic deformation is obtained by applying (2.12) and (2.13)

$$\dot{\mathbf{F}}^p = (\sum_{\alpha=1}^{N} \frac{\partial \psi_\alpha}{\partial \tau_\alpha} \mathbf{s}_\alpha \otimes \mathbf{m}_\alpha) \mathbf{F}^p \quad , \tag{2.21}$$

$$\dot{\gamma}_\alpha = -\frac{\partial \psi_\alpha}{\partial g_\alpha} = \frac{\partial \psi_\alpha}{\partial \tau_\alpha} \quad . \tag{2.22}$$

It is apparent that the flow rule for the plastic deformations is that introduced by Rice [21], i.e.,

$$\dot{\mathbf{F}}^p = (\sum_{\alpha=1}^{N} \dot{\gamma}_\alpha \mathbf{s}_\alpha \otimes \mathbf{m}_\alpha) \mathbf{F}^p \quad , \tag{2.23}$$

where α is a summation over all crystallographic slip systems.

In this work, slip is regarded as irreversible and thus,

$$\dot{\gamma}_\alpha \geq 0 \quad . \tag{2.24}$$

For reference the 12 slip systems of FCC crystals are given in table 2.1. Since the systems are considered irreversible, there are 24 systems for FCC crystals in this model.

Table 2.1. *FCC slip systems*

System	**A2**	**A3**	**A6**	**B2**	**B4**	**B5**
$s * \sqrt{2}$	$\pm[0\bar{1}1]$	$\pm[101]$	$\pm[110]$	$\pm[0\bar{1}1]$	$\pm[\bar{1}01]$	$\pm[\bar{1}10]$
$m * \sqrt{3}$	$(\bar{1}11)$	$(\bar{1}11)$	$(\bar{1}11)$	(111)	(111)	(111)
System	**C1**	**C3**	**C5**	**D1**	**D4**	**D6**
$s * \sqrt{2}$	$\pm[011]$	$\pm[101]$	$\pm[\bar{1}10]$	$\pm[011]$	$\pm[\bar{1}01]$	$\pm[110]$
$m * \sqrt{3}$	$(\bar{1}\bar{1}1)$	$(\bar{1}\bar{1}1)$	$(\bar{1}\bar{1}1)$	$(1\bar{1}1)$	$(1\bar{1}1)$	$(1\bar{1}1)$

Assuming rate-independent slip and minimizing the deformation energy, it is shown in [7] that the slip rates and stresses can be restricted to Kuhn-Tucker form [22] as

$$\tau_\alpha - g_\alpha \leq 0, \quad \dot{\gamma}_\alpha \geq 0, \quad (\tau_\alpha - g_\alpha)\dot{\gamma}_\alpha = 0 \tag{2.25}$$

These conditions provide an optimization technique and all the traditional constraints for rate-independent plasticity. Namely, that the material remain elastic, with plastic deformation occurring only when critical resolved shear stresses are reached; and that slip is irreversible. A strain rate dependent model could be developed by including a strain-rate dependent evolution of plastic deformation (see e.g. Bronkhorst et al. [16] or Cuitino and Ortiz [15] as well as others).

It is also noted from (2.11) that

$$W^p = \sum_{\alpha=1}^{N} \int_{t=0}^{t} \tau_\alpha[t]\dot{\gamma}_\alpha[t]dt \quad . \tag{2.26}$$

The material tangent when a single slip system is active is

$$\mathcal{C}^{\alpha}_{iJkL} = C^{e}_{iMkN}(F^{p})^{-1}_{JM}(F^{p})^{-1}_{LN} - C^{mixed}_{iJ\alpha}C^{mixed}_{kL\alpha}\frac{1}{\partial(\tau_\alpha - \tau^{c}_{\alpha})/\partial\gamma_\alpha} \quad , \tag{2.27}$$

where

$$\begin{aligned} \mathcal{C}^{mixed}_{ij\alpha} &= \mathcal{C}^{e}_{imab}F^{e}_{aq}s^{\alpha}_{q}(F^{p})^{-T}_{mj}m^{\alpha}_{b} \\ &\quad + P^{e}_{im}(F^{p})^{-1}_{jq}s^{\alpha}_{q}m^{\alpha}_{m} \quad , \end{aligned} \tag{2.28}$$

and with the assumptions $\frac{\partial\gamma_\alpha}{\partial(\tau_\alpha - \tau^{c}_{\alpha})} = 1/\frac{\partial(\tau_\alpha - \tau^{c}_{\alpha})}{\partial\gamma_\alpha}$ and that $\mathbf{s}\cdot\mathbf{m} = 0$.

2.3 Numerical Implementation

It is easiest to define all tensors in the crystal frame. No equations refer to the lab frame in this paper. Obviously, the results must be rotated back to the lab frame, and inputs from the lab frame must be rotated into the crystal frame when this material model is implemented for multiple crystal orientations. Working in the crystal frame simplifies many equations as crystal material properties are easier to express in the crystal frame, such as $\mathbf{s}$, $\mathbf{m}$, and $\mathcal{C}$. Thus, there are only two frames of reference, the undeformed crystal and the deformed crystal.

2.3.1 Incremental Deformation Steps

Time discretization is done assuming that boundary conditions will be enforced at discrete time steps, $t_0, t_1, ..., t_n, t_{n+1}, ...$ The subscript n and $n+1$ will be used to distinguish values at specific time steps.

2.3.2 Elastic

The only required input to the elastic model is the elastic deformation gradient, $\mathbf{F}^e_{n+1}$. Elastic deformation does not have a path dependency and as there is no time dependence in the elastic model, the time discretization does not need any discussion.

2.3.3 Crystal Single Slip

First take

$$\Delta\gamma = {}_{n+1}\gamma_\alpha - {}_n\gamma_\alpha \quad , \tag{2.29}$$

then from an exponential mapping of equation (2.23)

$${}_{n+1}\mathbf{F}^p = (\mathbf{I} + \sum_{\alpha=1}^{N} \Delta\gamma_\alpha \mathbf{s}_\alpha \otimes \mathbf{m}_\alpha)_n\mathbf{F}^p \quad . \tag{2.30}$$

Lastly,

$${}_nW^p = \sum_{\alpha=1}^{N} ({}_n\tau_\alpha)({}_n\gamma_\alpha) \quad , \tag{2.31}$$

from (2.26).

Single slip is solved by iteration over ${}_{n+1}\gamma_\beta$, and equations (2.30) to solve for ${}_{n+1}\mathbf{F}^p$ and (2.6) to solve for ${}_{n+1}\mathbf{F}^e$. The resolved shear stress is computed by passing ${}_{n+1}\mathbf{F}^e$ to the elastic model to obtain ${}_{n+1}\mathbf{P}$ and using equation (2.19). The value of ${}_{n+1}\gamma_\beta$ can be found by using an iterative method such as a Newton-Raphson until the Kuhn-Tucker conditions (equations (2.25)) are satisfied, i.e., the resolved sheer stress equals the critical resolved shear stress or in the simplest case, only an elastic reaction occurs.

It should be noted that these values are strictly incremental, yielding a path-dependent nature to the evolution of the material.

A system of allowing only single slip (infinite latent hardening) is adopted. An energy for each possible slip system is determined and the minimum energy system selected, thus determining the active slip system. Note that once a slip system is activated, it will be the only slip system active in that spatial portion of material for all future time steps. As will be introduced in the next chapter, the material can escape this restriction only by forming microstructures of multiple single slip regions. This convention is due to the work of Ortiz and Repetto [7] and Conti and Ortiz [1] in which it was shown that when using a slip model involving discrete crystal slip systems with a strong latent hardening matrix, local single slip provides energy wells in the energy of deformation. Thus, with this model the lowest energy available to accommodate a deformation is always a microstructure of single slip volumes.

Assuming a given slip system, the single slip model takes four inputs: the final deformation for the deformation step, ${}_{n+1}\mathbf{F}$; the previous step's plastic deformation, ${}_{n}\mathbf{F}^{p}$; the total accumulated slip strain at the end of time step n, ${}_{n}\gamma_{\beta}$; and the current mean free path length of the dislocations, ${}_{n+1}h_{\beta}$. The mean free paths and how they are obtained are discussed in section 3.3.1. The total energy density, ${}_{n+1}W$, stress state, ${}_{n+1}\mathbf{P}$, and updated state variables, ${}_{n+1}\mathbf{F}^{p}$ and ${}_{n+1}\gamma_{\beta}$ need to be computed. The subscript β is maintained to designate these equations are for a single slip system. The total discretized energy density is defined as

$$ {}_{n+1}W = {}_{n+1}W^{e} + {}_{n+1}W^{p} \quad , \tag{2.32} $$

which is introduced to replace ϕ in order to keep the symbols uniform for the discretized variables. As derived by Aubrey and Ortiz [10], the dislocation wall energy has the effect of

increasing the critical resolved shear stress as

$$ {}_{n+1}\tau_\beta^c = \tau_o^c + \frac{T}{b\ {}_{n+1}h_\beta} \quad , \tag{2.33} $$

where T is the dislocation line tension (assumed constant in this work) and b is the Burgers vector.

Given the value of ${}_{n+1}\tau_\beta^c$, the energy can then be computed from equations (2.7), (2.17), and (2.31) and the stress from (2.9) and (2.16). Obviously the summing operation in (2.31) for the plastic energy only includes the single active slip system β as all other $\gamma_\alpha = 0$.

2.3.4 Crystal Coplanar Slip

Due to the fact that two coplanar slip systems form a laminate microstructure in which the two planes of dislocations do not interact and in which the separation between physical regions of single slip lack dislocation walls which inhibit further slip, it is desirable to create a theory which does not distinguish between coplanar slip regions. Otherwise further hardening falsely occurs when a coplanar laminate microstructure activates further children systems. In theories which include more traditional work hardening, it is apparent that coplanar hardening is much closer in magnitude to self hardening than other forms of latent hardening [23, 2, 24]. To understand the details of the motivation for a coplanar model, it is required to understand the laminate model that is discussed in the following chapter [cf. Chapter 3]. The reader is referred to that material for details.

Due to the unique geometric nature of coplanar slip, multiple active coplanar slip systems can be treated as a single active slip system on a common plane. This is accomplished by

defining an effective slip direction as a combination of the coplanar slip directions.

$$ {}_n\hat{\mathbf{s}} \equiv \sum_{\alpha \in coplanar} \frac{{}_n\dot{\gamma}_\alpha}{{}_n\dot{\gamma}_T} s_\alpha \quad , \tag{2.34} $$

where ${}_n\dot{\gamma}_T \equiv \sum_{\alpha \in coplanar} {}_n\dot{\gamma}_\alpha$.

Using this definition of $\hat{\mathbf{s}}$ the values of the plastic deformation gradient, stress, and plastic work energy (and thus, total energy) are equivalent to activating the slip systems simultaneously. Only the material tangent used in solution iterations needs additional work. These are shown subsequently.

As the coplanar slip model increases the degrees of freedom in the laminate it creates new variables for the slip strains on each plane. These are solved by imposing the condition

$$ {}_n\tau_\alpha = {}_n\tau^c \; for \; all \; \alpha \in \; coplanar \quad . \tag{2.35} $$

Solving for the coplanar slip strains, ${}_n\gamma_\alpha$, when this condition is met is simplified by considering that the minimum energy deformation in FCC crystals allows for a maximum of two slip systems to be active during a single time step. Activating the third FCC slip system drives the combined total deformation down, while increasing slip. Solving for condition (2.35) requires a sequence of steps to implement as it is unknown which slip systems activate or if single or multiple slip is active. The solution steps follow:

1. Compute all $\tau_\alpha - \tau^c$

2. Activate maximum $\tau_\alpha - \tau^c$ slip system from step 1 as single slip

3. Recompute all $\tau_\alpha - \tau^c$

   if all $\tau_\alpha - \tau^c \leq 0, exit$

else, return max slip system to original slip strain and activate two highest $\tau_\alpha - \tau^c, exit.$

Applying the condition to multiple coplanar slip requires a good initial guess and an iteration. The initial guess, $\hat{\mathbf{s}}_0$, can be computed using the values of the initial shear stress on the slip systems and assuming $\mathbf{F}^e \approx \mathbf{I}$

$$\hat{\mathbf{s}}_0 = \frac{(\omega_1 - \omega_2 d)}{(\omega_1 + \omega_2)(1-d)}\mathbf{s}_1 + \frac{(\omega_2 - \omega_1 d)}{(\omega_1 + \omega_2)(1-d)}\mathbf{s}_2 \quad , \tag{2.36}$$

where

$$\omega_\alpha = \tau_\alpha - \tau_\alpha^c \quad , \tag{2.37}$$

$$d = \mathbf{s}_1 \cdot \mathbf{s}_2 \quad . \tag{2.38}$$

Note $d = 1/2$ for FCC crystal systems.

Due to the approximations, this initial guess does not yield all $\tau_\alpha - \tau^c = 0$ for all actives systems, α, but can further be quickly driven to the exact solution by an iterative algorithm such as Newton-Raphson. The required derivative for such an algorithm is

$$\frac{\partial_n \tau_\alpha - {}_n\tau_\alpha^c}{\partial \gamma_\beta} = -({}_n\mathbf{F}^e\mathbf{s}_\alpha \otimes \mathbf{m}_\alpha) \cdot \mathcal{C}^e \cdot ({}_n\mathbf{F}^e\mathbf{s}_\beta \otimes \mathbf{m}_\beta) \quad . \tag{2.39}$$

Note that "$\cdot$" above sums over two indices as previously defined, hence the left-hand side is a scalar. The derivation of the above takes advantage of the fact that because $\mathbf{m} \cdot \mathbf{s} = 0$, then $({}_nF^p)({}_{n+1}F^p)^{-1} = \mathbf{I}$.

Using this definition of $\hat{\mathbf{s}}$ (2.34), the plastic work is equivalent to using the total slip

strain.

$$\Delta_n W^p = \sum_\alpha ({}_n\tau^c_\alpha)(\Delta_n \gamma_\alpha) \quad , \tag{2.40}$$

where $\Delta_n \gamma_\alpha \equiv {}_n\gamma_\alpha - {}_{n-1}\gamma_\alpha$. Using the fact that all ${}_n\tau^c_\alpha$ are identical in a laminate with coplanar slip

$$\Delta_n W^p = ({}_n\tau^c)(\Delta_n \gamma_T) \quad , \tag{2.41}$$

which yields the desired result that the plastic work energy is equivalent.

For multiple activated coplanar systems, the plastic deformation gradient can also be treated with an equivalent slip direction. To signify that the slip in the following equations is coplanar, the subscript on $\mathbf{m}$ is dropped. For multiple simultaneous slip systems

$${}_n\mathbf{F}^p_l = (\mathbf{I} + \sum_\alpha {}_n\gamma_\alpha \ \mathbf{s}_\alpha \otimes \mathbf{m})({}_{n-1}\mathbf{F}^p_l) \quad . \tag{2.42}$$

If instead a single slip system is activated with direction $\hat{\mathbf{s}}$ and shear strain γ_T

$$\begin{aligned} {}_n\mathbf{F}^p_l &= (\mathbf{I} + {}_n\gamma_T \ \hat{\mathbf{s}} \otimes \mathbf{m})({}_{n-1}\mathbf{F}^p_l) \\ &= (\mathbf{I} + (\sum_\alpha {}_n\gamma_\alpha \ \mathbf{s}_\alpha) \otimes \mathbf{m})({}_{n-1}\mathbf{F}^p_l) \\ &= (\mathbf{I} + (\sum_\alpha {}_n\gamma_\alpha \ \mathbf{s}_\alpha \otimes \mathbf{m}))({}_{n-1}\mathbf{F}^p_l) \quad . \end{aligned} \tag{2.43}$$

It is also noted that if coplanar slip systems are activated sequentially this is also true

$$\begin{aligned} {}_n\mathbf{F}^p_l &= {}_n\mathbf{F}^p_2 \, {}_n\mathbf{F}^p_1({}_{n-1}\mathbf{F}^p_l) \\ &= (\mathbf{I} + {}_n\gamma_2 \ \mathbf{s}_2 \otimes \mathbf{m})(\mathbf{I} + {}_n\gamma_1 \ \mathbf{s}_1 \otimes \mathbf{m})({}_{n-1}\mathbf{F}^p_l) \\ &= (\mathbf{I} + (\sum_\alpha {}_n\gamma_\alpha \ \mathbf{s}_\alpha \otimes \mathbf{m}))({}_{n-1}\mathbf{F}^p_l) \quad , \end{aligned} \tag{2.44}$$

where the last step in (2.44) is recognizing that all cross terms in $(\sum_\alpha {}_n\gamma_\alpha \mathbf{s}_\alpha) \otimes \mathbf{m}_\alpha$ and $(\mathbf{I} + {}_n\gamma_2 \mathbf{s}_2 \otimes \mathbf{m})(\mathbf{I} + {}_n\gamma_1 \mathbf{s}_1 \otimes \mathbf{m})$ cancel due to $\mathbf{s} \cdot \mathbf{m} = 0$ for coplanar systems.

The stress is unaffected since it is a function only of $\mathbf{F}$ and $\mathbf{F}^p$.

The material tangent for active coplanar slip does not conform to the single slip equation when using $\hat{\mathbf{s}}$. It is

$$\mathcal{C}^{coplanar}_{iJkL} = \mathcal{C}^{e}_{iMkN}(F^p)^{-T}_{MJ}(F^p)^{-T}_{NL} - \sum_\alpha \sum_\beta \frac{C^{mixed}_{iJ\alpha} C^{mixed}_{kL\beta}}{\frac{\partial(\tau_\beta - \tau^c_\beta)}{\partial \gamma_\alpha}} \quad , \tag{2.45}$$

where the sum over α and β is for the active slip systems, since by definition $\frac{\partial \gamma_\alpha}{\partial(\tau_\beta - \tau^c_\beta)} = 0$ if $\tau^c_\beta > \tau_\beta$. In practice, it is more tractable to implement the single slip material tangent (equation (2.27)) using $\hat{\mathbf{s}}$ for the slip direction. Although not exact, it still provides convergence within a reasonable number of iterations without excessive computation of $\mathbf{C}^{mixed}$ values. It should also be mentioned that if the active slip systems change, then there are corresponding discontinuities in the material tangent.

The preceding coplanar slip theory allows for the treatment of coplanar slip in a manner identical to that used for single slip.

Chapter 3

Laminate Microstructures

Under the assumption of infinite latent hardening, the only way for a material to activate multiple slip systems is to divide into spatial volumes with different single slip systems. Previous work [7, 1] has provided evidence that with strong latent hardening the energy of single slip is an energy well and is always less than multiple slip in energy considerations. Following previous work [7, 9, 10] microstructures of single slip regions will be introduced when the energy of the microstructure is less than the energy of single slip (or purely elastic deformation). This work deviates from previous works by introducing coplanar slip laminates and in the calculation of the laminate length scale from the nonlocal energy terms.

Following the previous work of Ortiz, Repetto, and Stainier [9], a formulation of laminate microstructures is used. These are used due to the inability to resolve minimum energies for any general microstructure [10], but the work of Ortiz and Repetto [7] show that many dislocation structures found in experiments can be reproduced using sequential laminate structures. The theory of sequential laminates used here is covered by Kohn [25] and reviewed in other references [10, 7]. A summary will be given here along with extensions to the nonlocal energy. Specifically dislocation mean free path length, evolution of laminate thickness, and notes on the dislocation wall normals are added to the theory.

Another advantage of using laminate structures is that complex structures can be formed

by embedding simple laminate structures inside previously formed laminate structure. A simple laminate is defined as a repetitive sequence of two layers of material. As embedded simple laminate structures look the same at any level, one only needs to describe and analyze the case of a single simple laminate, which can then be layered into more complicated structures. These are described as ranks by Kohn. Each set of layers will be referred to as a "laminate" (the use of node from previous works is changed to avoid future confusion with finite element nodes). Note that the term "laminate" is not referring to a single laminate layer, but to the set of similar layers. (E.g. the set of grey bands in figure 3.2 are one laminate.) A laminate which has branched is called a "branch," and one which has not branched is called a "leaf." Each branch will have two "children." Every laminate except the rank 0 initial material will have one "sibling" and one "parent." The following notation for laminate designation is given in figure 3.1. The indice l will be used to refer to a unspecified laminate, with l^+ and l^- being the children of l and l_p being the parent of l. Note that each branch is identical, having one single slip system active in itself and dividing into a simple laminate structure with two slip systems. (In this work one of the slip systems is restricted to being the same as the parent.) Hence, the complex laminate structure can be formed by an embedded composition of simple laminates. See figure 3.2 for an illustration of a grain with a rank two laminate subgrain structure.

Note that each laminate has only one active slip system, and thus the single slip model is used for individual laminate deformation. Also, since a laminate has only one active slip system the indice α used in the single slip section can be replaced by l without modifying the equations.

A branched laminate is defined by the slip system active on each side, $\alpha_{l^\pm}$, combined laminate thickness L_l^c, the normal to the dislocation wall dividing the two laminates, $\mathbf{N}_l$,

the volume fraction of each laminate, $\lambda_{l^\pm}$, and the jump of the deformation across the wall, $\mathbf{a}_l$ (cf. figure 3.3). One of the subtleties in the laminate theory is the evolution of the laminate parameters. These will be further discussed in the evolution section, but for ease in understanding the full work, those that evolve are given a time subscript n in this section, namely ${}_nL_l^c$ and ${}_n\mathbf{a}_l$. The parameters $\mathbf{N}_l$ and $\lambda_{l^\pm}$ are not evolved.

Note that the active slip systems within each laminate are not evolved. Thus, once a laminate forms, it always remains in the microstructure although it can further branch within itself. This provides the theory with path dependency.

The framework for the laminate structures needs to be presented before nonlocal energy terms can be understood, but the nonlocal terms will effect the laminate framework. Rather than showing the general equations for the laminates and then modifying them later to contain the nonlocal terms, the nonlocal terms are included without a full explanation and derived in the next section. The section ends with a discussion of equilibrating the structure and accounting for the stress jumps when new laminates form. Equilibration now includes the laminate thickness providing an accurate form of evolving slip hardening.

3.1 Laminate Variable Properties

As the deformation must be rank one connected

$$ {}_n\mathbf{F}_{l^+} - {}_n\mathbf{F}_{l^-} = {}_n\mathbf{a}_l \otimes \mathbf{N}_l \quad , \tag{3.1} $$

where $\{{}_n\mathbf{a}_l, \mathbf{N}_l\} \in \Re^3$ and as $\mathbf{N}_l$ is a unit vector indicating direction, $\|\mathbf{N}\| = 1$. The symbol ${}_n\mathbf{a}_l$ is the polarization vector which varies with the values of the deformation gradient.

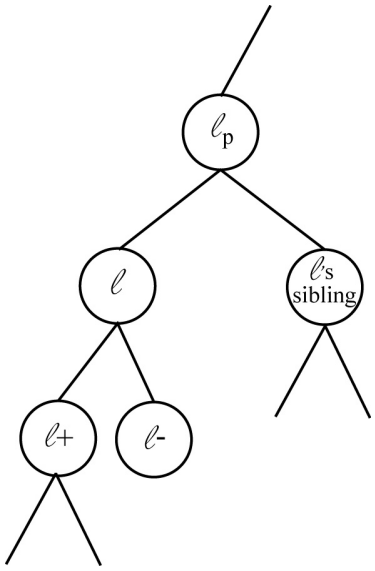

Figure 3.1. *Labels used on laminate subgrain structures*

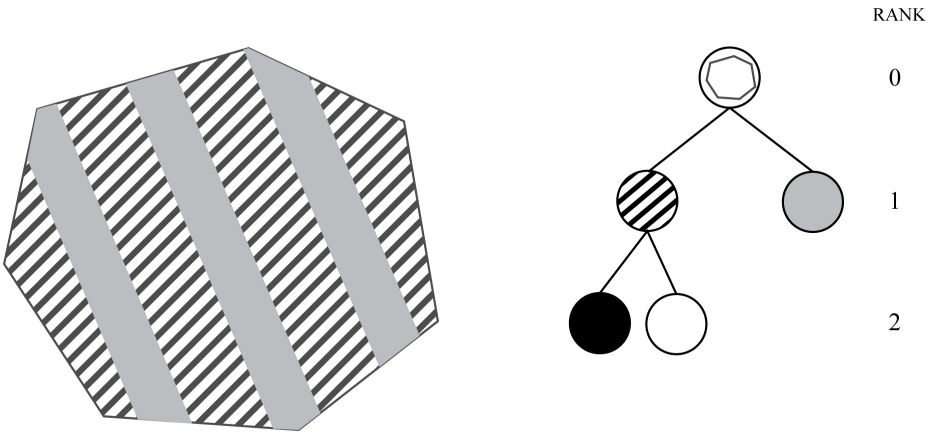

Figure 3.2. *Illustration of a grain with a rank two subgrain laminate structure. Shading in tree structure corresponds to structure shown in grain illustration*

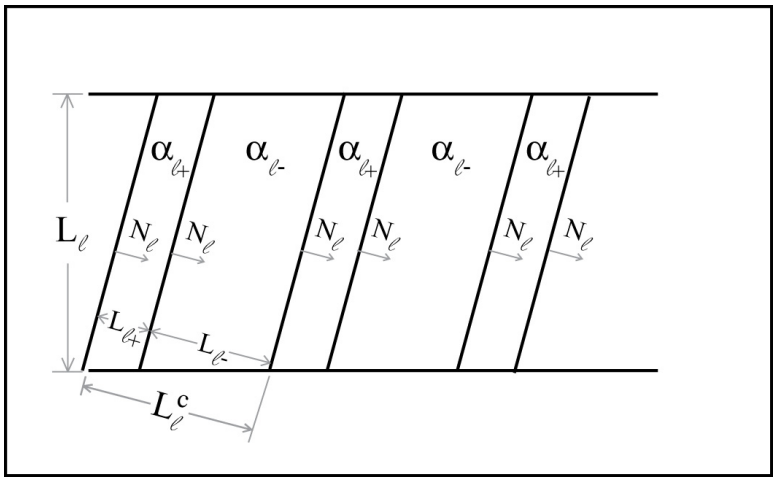

Figure 3.3. *Simple laminate structure variables. Illustration is not to scale.*

Obviously, the volume fractions, $\lambda_l \in \Re$. Note that λ_l must obey the rules

$$\lambda_{l^+} + \lambda_{l^-} = 1, \quad \lambda_{l^\pm} \in [0,1] \quad . \tag{3.2}$$

Given the volume fraction, the average or macroscopic deformation of the laminate follows as

$${}_n\mathbf{F}_l = (\lambda_{l^-})({}_n\mathbf{F}_{l^-}) + (\lambda_{l^+})({}_n\mathbf{F}_{l^+}) \quad . \tag{3.3}$$

From (3.1) and (3.3), the deformation gradient of the children can be written

$${}_n\mathbf{F}_{l^\pm} = ({}_n\mathbf{F}_l) \pm \lambda_{l^\mp}({}_n\mathbf{a}_l \otimes \mathbf{N}_l) \quad . \tag{3.4}$$

The references [10, 9, 7, 17] derive the relationship

$${}_n\mathbf{P}_l = (\lambda_{l^-})({}_n\mathbf{P}_{l^-}) + (\lambda_{l^+})({}_n\mathbf{P}_{l^+}) \quad , \tag{3.5}$$

and the material tangent for a branched laminate

$$ {}_n\mathcal{C}_l^{laminate} = (\lambda_{l^+})({}_n\mathcal{C}_{l^+}^{s.s.}) + (\lambda_{l^-})({}_n\mathcal{C}_{l^-}^{s.s.}) \quad , \tag{3.6} $$

where equation (2.27) is used to calculate ${}_n\mathcal{C}_{l^\pm}^{s.s.}$.

The characteristic width of a laminate's layers is the combined width of the two children's layers,

$$ {}_nL_l^c \equiv {}_nL_{l+} + {}_nL_{l-} \quad . \tag{3.7} $$

Due to the repetitive planar geometry of a laminate structure, the width of a child laminate's layers is related to its parent layer's width by the volume fraction

$$ {}_nL_{l^\pm} = \lambda_{l^\pm}\ {}_nL_l^c \quad . \tag{3.8} $$

A laminate's characteristic width, ${}_nL_l^c$, is further restricted to be less than the width of the parent structure

$$ {}_nL_l^c \leq {}_nL_{l_p} \quad . \tag{3.9} $$

Note that this restriction has been added in this work as it was found that energy minimization alone allowed for the non-physical case of children larger than the parent.

When a laminate branches and becomes a parent the plastic deformation that has occurred in the parent during previous time steps is retained as this deformation is permanent and has already occurred. The children accommodate any remaining deformation. The current plastic deformation in the parent (e.g., ${}_{n-1}\mathbf{F}_l^p$) will not continue to evolve with further deformation after the children laminates are formed. The macroscopic deformation, ${}_n\mathbf{F}_l$, will evolve as the laminates continue deforming (cf. equation (3.3)). To account for this

when a laminate forms its initial plastic deformation is set equal to its parent's previous plastic deformation

$$ {}_{n-1}\mathbf{F}^p_{l^+} = {}_{n-1}\mathbf{F}^p_l \quad , \tag{3.10} $$

so that by equation (2.30)

$$ {}_n\mathbf{F}^p_{l^+} = (\mathbf{I} + \Delta\gamma_{l^+}\hat{\mathbf{s}}_{l^+} \otimes \mathbf{m}_{l^+})_{n-1}\mathbf{F}^p_l \quad , \tag{3.11} $$

the correct elastic deformation is given by equation (2.6), ${}_n\mathbf{F}^e_{l^+} = {}_n\mathbf{F}({}_n\mathbf{F}^p_{l^+})^{-1}$. The slip strain of the children is set to zero, ${}_{n-1}\gamma_{l^+} = 0$, so that the incremental plastic energy is correctly computed.

3.2 Branching Energy Computation

To establish a simple laminate structure's energy, the minimum possible energy for the laminate structure should be found in order to make comparisons to the single slip and elastic energies. Thus, one finds the solution to

$$ {}_nW_l[{}_n\mathbf{F}_l] \equiv \min_{\alpha_{l^\pm}, a_l, N_l, \lambda_{l^\pm}, L^c_l} \left(\lambda_{l^-}\ {}_nW_{l^-} + \lambda_{l^+}\ {}_nW_{l^+} + \left({}_{(n-1)}\tau_l\right)\left({}_{(n-1)}\gamma_l\right) + 2\Upsilon \frac{{}_nL^c_l}{{}_{n-1}L_l} {}_nW^{BL}_l \right) \quad , \tag{3.12} $$

Υ is the depth of the boundary layer, reference section 3.3.2 for details. This minimum is the energy density of laminate l branching and becoming the two leaves l^+ and l^-. If this energy is less than the single slip (or elastic) energy, the laminate forms. The first term is the energy from the laminate l^-, both the elastic W^e and plastic W^p. The second term is likewise the energy from laminate l^+. The third term is the plastic energy that the

possibly branching laminate l has already stored by single slip; it is included in the branched energy in order to make accurate comparisons to the energy of single slip. Note the energy accumulated in this term has already been completed in the previous deformation step, and due to the assumed irreversibility does not evolve further; thus, it can be removed from this minimization as a constant. The fourth term is the boundary layer energy caused by the misfit between the laminates and the boundaries of the parent system; it will be discussed in section 3.3.2.

Note that the previous work of Aubrey and Ortiz [10] treated the nonlocal energy terms of the boundary layer and the dislocation walls as perturbations of the energy, so were not directly included in the minimization (eqn. (3.12)). When the nonlocal energy is introduced later, it will be estimated to show that it should not be treated as a perturbation, but minimized directly.

3.2.1 Slip Plane Selection, α

The possible slip planes will be iterated over to find a minimum deformation energy with respect to $\alpha_{l\pm}$. This reduces the required solution to eqn. (3.12) to finding

$$
\begin{aligned}
&{}_nW_l[{}_n\mathbf{F}_l]_{\alpha^*_{l\pm}} = \left({}_{(n-1)}\tau_l\right)\left({}_{(n-1)}\gamma_l\right) + \\
&\min_{a_l,N_l,\lambda_{l\pm},L^c_l}\left(\lambda_{l^-}\ {}_nW_{l^-} + \lambda_{l^+}\ {}_nW_{l^+} + 2\Upsilon\frac{{}_nL^c_l}{{}_{n-1}L_l}{}_nW^{BL}_l\right) \quad ,
\end{aligned}
\tag{3.13}
$$

for a given set of two slip planes $\alpha^*_{l^+}$ and $\alpha^*_{l^-}$ using the given restrictions.

3.2.2 Dislocation Wall Normals, N

The complexity of calculating the wall normal when only single slip is active can be reduced by referring to work done by Ortiz and Repetto [7], although care must be taken in how

these are implemented. Ortiz and Repetto tabulated wall normals using rank one compatibility of deformation assuming only plastic single slip on each side of a rank one laminate with no elastic deformation for FCC crystal systems. Under the plausible assumption that near the dislocation wall the majority of deformation is plastic, as little distance exists for elastic deformation, these derived plastic deformation wall normals can be assumed a good approximation. However, two details must be considered when implementing these directly from the reference. First, they were derived in the Eulerian reference frame and second, the length evolution of the wall normal degenerate cases, i.e., those cases for which the slip system normals or slip system directions are identical. Note that in the derivation of the wall normals there is also a restriction placed on the ratio $\dot{\gamma}^+/\dot{\gamma}^-$, which is not directly applied in this work. This again relates to the assumption that all the deformation contained in the compatible wall is plastic, while elsewhere, elastic deformation eases any restriction.

Although the conversion of the Lagrangian reference frame normal $\mathbf{N}$ to the Eulerian reference frame normal $\mathbf{n}$ is given in the reference,

$$\mathbf{n} = \frac{(\mathbf{F}_{l^+})^{-T}\mathbf{N}_l}{\|(\mathbf{F}_{l^+})^{-T}\mathbf{N}_l\|} \quad , \tag{3.14}$$

some explanation is beneficial. A similar expression with $\mathbf{F}^-$ can be derived following the same steps, yielding

$$\mathbf{N}_l = \frac{(\mathbf{F}_{l^+})^T\mathbf{n}_l}{\|(\mathbf{F}_{l^+})^T\mathbf{n}_l\|} = \frac{(\mathbf{F}_{l^-})^T\mathbf{n}_l}{\|(\mathbf{F}_{l^-})^T\mathbf{n}_l\|} \quad . \tag{3.15}$$

Although it appears that two different deformations, $\mathbf{F}_{l^+}$ and $\mathbf{F}_{l^-}$, are applied to the same wall normal $\mathbf{n}_l$ to yield $\mathbf{N}_l$; a better understanding is gained by applying polar decomposition to the deformation gradients. By polar decomposition $\mathbf{F}$ can be split multiplicatively into a

symmetric stretch tensor $\mathbf{U} = \sqrt{\mathbf{F}^T\mathbf{F}}$ and an orthogonal rotation $\mathbf{R} = \mathbf{F}\mathbf{U}^{-1}$

$$\mathbf{N}_l = \frac{\mathbf{U}_{l^+}(\mathbf{R}_{l^+})^T\mathbf{n}_l}{\|\mathbf{U}_{l^+}(\mathbf{R}_{l^+})^T\mathbf{n}_l\|} = \frac{\mathbf{U}_{l^-}(\mathbf{R}_{l^-})^T\mathbf{n}_l}{\|\mathbf{U}_{l^-}(\mathbf{R}_{l^-})^T\mathbf{n}_l\|} \quad , \tag{3.16}$$

since $\left\|(\mathbf{R}^{\pm})^T\mathbf{n}\right\| = 1$ and $\mathbf{U}$ is a symmetric tensor (and thus diagonalizable by choice of reference frame)

$$\mathbf{N}_l = (\mathbf{R}_{l^+})^T\mathbf{n}_l = (\mathbf{R}_{l^-})^T\mathbf{n}_l = \frac{(\mathbf{F}_l)^T\mathbf{n}_l}{\|(\mathbf{F}_l)^T\mathbf{n}_l\|} \quad . \tag{3.17}$$

Thus, the conversion between $\mathbf{n}$ and $\mathbf{N}$ is only the rotation involved in the deformation and must be equal for both sides as well as at the global level for compatibility of the deformation at the dislocation wall.

From Ortiz and Repetto [7], the branched laminate composed of the two slip systems α_{l^+} and α_{l^-} has only two possible wall normal orientations if the slip systems are not degenerate, i.e., the slip directions are not identical or the slip planes are not identical. These two possibilities for wall normal direction can then be iterated over and only the lower energy taken.

For the degenerate case in which the slip directions are equal it can be shown that

$$\mathbf{n}_l = \frac{\dot{\gamma}_{l^+}\mathbf{m}_{l^+} - \dot{\gamma}_{l^-}\mathbf{m}_{l^-}}{\|\dot{\gamma}_{l^+}\mathbf{m}_{l^+} - \dot{\gamma}_{l^-}\mathbf{m}_{l^-}\|} \quad . \tag{3.18}$$

Thus, the normal belongs to a 2D unit circle which contains $\mathbf{m}_{l^+}$ and $\mathbf{m}_{l^-}$. This unit circle is iterated over by taking a set angle interval. The normal with the lowest energy is selected. Note since the opposite of the normal gives an identical wall orientation, only half of the circle needs to be checked. (If $\mathbf{N}_l \rightarrow -\mathbf{N}_l$, then $\mathbf{a}_l \rightarrow -\mathbf{a}_l$, and the calculations are not

affected.) Also, the system slip directions, $\mathbf{m}^+$ and $\mathbf{m}^-$ may be excluded as those directions are identical to only a single slip system activated.

For the degenerate cases in which the slip plane normals are identical,

$$\mathbf{n}_l = \mathbf{m}_{l^+} = \mathbf{m}_{l^-} \quad . \tag{3.19}$$

Due to the parallel slip planes the dislocations of these two systems will not interact and will not form a dislocation wall. This and other considerations for the wall normal in this section were noted by Ortiz and Repetto [7], but were not considered in the initial theory of Aubrey and Ortiz [10]. Coplanar slip systems were already discussed in section 2.3.4.

Unfortunately, these conditions only hold for single slip. In considering the formation of laminates in which more than one slip system is activated on each side of the wall normal (e.g., two coplanar slip systems), there is presently no alternative but to search the unit sphere of all wall normals for the lowest energy wall normal.

As described, the set of all possible $\mathbf{N}_l$ can now be iterated over, thus reducing the minimization of (3.13) to finding

$$\begin{aligned} {}_nW_l[{}_n\mathbf{F}_l]_{\alpha^*_{l^\pm},\mathbf{N}^*_l} &= \left({}_{(n-1)}\tau_l\right)\left({}_{(n-1)}\gamma_l\right) \\ &+ \min_{\mathbf{a}_l,\lambda_{l^\pm},L^c_l} \left(\lambda_{l^-}\ {}_nW_{l^-} + \lambda_{l^+}\ {}_nW_{l^+} + 2\Upsilon \frac{{}_nL^c_l}{{}_{n-1}L_l} {}_nW^{BL}_l \right) \quad . \end{aligned} \tag{3.20}$$

When considering single slip activation, the set of possible wall normals considered is reduced using compatibility.

3.2.3 Computation of Volume Fraction, λ

As there are strict bounds limiting λ to the domain $\lambda \in [0,1]$, a discrete minimization of λ can be conducted. Note the endpoints of the domain can be avoided as they pertain to single slip. Using an accuracy of 0.1, λ_l is given the possible set of values

$$\lambda_l \in \{0.1, 0.2, 0.3, 0.4, 0.5, 0.6, 0.7, 0.8, 0.9\} \quad .$$

All that is lost in this approach of solving for λ is accuracy in the volume fraction of the laminate.

It is possible a more computationally efficient solution would simultaneously solve for λ, $\mathbf{a}$, and L^c, but the discrete optimization is much more timely to implement.

The minimization equation 3.20 is now reduced to

$$\begin{aligned} {}_nW_l[{}_n\mathbf{F}_l]_{\alpha^*_{l\pm},\mathbf{N}^*_l,\lambda^*_{l\pm}} &= \left({}_{(n-1)}\tau_l\right)\left({}_{(n-1)}\gamma_l\right) \\ &+ \min_{\mathbf{a}_l, L^c_l} \left(\lambda_{l^-}\ {}_nW_{l^-} + \lambda_{l^+}\ {}_nW_{l^+} + 2\Upsilon \frac{{}_nL^c_l}{{}_{n-1}L_l} {}_nW^{BL}_l\right) \quad . \end{aligned} \tag{3.21}$$

3.2.4 Computation of Polarization Vector, a

Minimization of (3.21) excluding the boundary layer energy with respect to $\mathbf{a}_l$ gives the condition that tractions must be compatible across dislocation walls:

$$({}_n\mathbf{P}_{l^+} - {}_n\mathbf{P}_{l^-})\mathbf{N}_l = \mathbf{0} \quad . \tag{3.22}$$

This is solved directly using a Newton-Raphson iteration for the value of $\mathbf{a}_l$. It will be shown that generally W^{BL}_l is small compared to the total plastic energy.

This minimization ideally should be done concurrently with the minimization of L_l^c as both effect the plastic energy, but currently a loop over the solutions of $\mathbf{a}_l$ and L_l^c is performed until convergence is reached. Convergence could be more efficient by the introduction of a minimization solution over $\mathbf{a}_l$ and L_l^c simultaneously. This analysis is difficult as the iteration in solving for $\gamma_{l\pm}$ prevents an analytical equation.

3.2.5 Computation of Laminate Thickness, L^c

With a given value for $\alpha_l^{\pm}$, λ_l, and N_l and the last iterative solution for $\mathbf{a}$, the solution for L_l^c is a simple analytical minimization. The value L_l^c only appears in the nonlocal terms as the addition to the critical resolved shear stress in the plastic energy and in the boundary layer energy. (The nonlocal energy is explained subsequently, but the minimization solution is placed here to be included with the other laminate parameter calculations.) The length scale of the laminates is derived through a competition between the two nonlocal energies. Specifically, using W^{DW} as the dislocation wall energy density and W^{BL} as the boundary layer energy density and W^{NL} as the total nonlocal energy density

$$
\begin{aligned}
{}_nW_l[{}_n\mathbf{F}_l]_{\alpha_{l\pm}^*,\mathbf{N}_l^*,\lambda_{l\pm}^*,\mathbf{a}_l^*} &= \left({}_{(n-1)}\tau_l\right)\left({}_{(n-1)}\gamma_l\right) \\
&+ \min_{L_l^c}\left(\lambda_{l^-}\ {}_nW_{l^-} + \lambda_{l^+}\ {}_nW_{l^+} + 2\Upsilon\frac{{}_nL_l^c}{{}_{n-1}L_l}{}_nW_l^{BL}\right) \\
&= \left({}_{(n-1)}\tau_l\right)\left({}_{(n-1)}\gamma_l\right) \\
&+ \min_{L_l^c}\left(\lambda_{l^-}\ (\tau_0^c)({}_n\gamma_{l^-}) + \lambda_{l^+}\ (\tau_0^c)({}_n\gamma_{l^+}) + {}_nW_l^{DW} + 2\Upsilon\frac{{}_nL_l^c}{{}_{n-1}L_l}{}_nW_l^{BL}\right) \\
&= \left({}_{(n-1)}\tau_l\right)\left({}_{(n-1)}\gamma_l\right) + \lambda_{l^-}\ (\tau_0^c)({}_n\gamma_{l^-}) + \lambda_{l^+}\ (\tau_0^c)({}_n\gamma_{l^+}) \\
&+ \min_{L_l^c}\left({}_nW_l^{DW} + 2\Upsilon\frac{{}_nL_l^c}{{}_{n-1}L_l}{}_nW_l^{BL}\right) \quad . \qquad (3.23)
\end{aligned}
$$

Thus the minimization with respect to ${}_nL_l^c$ is only over the nonlocal energy, ${}_nW_l^{NL}$. Substituting for the dislocation wall energy (equation (3.47))

$$\begin{aligned} {}_nW_l^{NL} &= \frac{T}{b\ {}_nL_l^c}\left(\frac{{}^n\gamma_{l^-}}{\zeta_{l^-}}\sqrt{1-(\mathbf{m}_{l^-}\cdot\mathbf{N}_l)^2}+\frac{{}^n\gamma_{l^+}}{\zeta_{l^+}}\sqrt{1-(\mathbf{m}_{l^+}\cdot\mathbf{N}_l)^2}\right) \\ &+ 2\Upsilon\frac{{}_nL_l^c}{{}_{n-1}L_l}{}_nW_l^{BL} \quad , \end{aligned} \tag{3.24}$$

ζ_l is the ratio of the dislocation mean free path length to the width of the laminate; it will be introduced in section 3.3.1.

The minimization with respect to ${}_nL_l^c$ then follows as

$${}_nL_l^c = \sqrt{\frac{T\ {}_{n-1}L_l}{2\Upsilon b\ {}_nW_l^{BL}}\left(\frac{{}^n\gamma_{l^-}}{\zeta_{l^-}}\sqrt{1-(\mathbf{m}_{l^-}\cdot\mathbf{N}_l)^2}+\frac{{}^n\gamma_{l^+}}{\zeta_{l^+}}\sqrt{1-(\mathbf{m}_{l^+}\cdot\mathbf{N}_l)^2}\right)} \quad , \tag{3.25}$$

the symbol ${}_{n-1}L_l$ is used rather than ${}_nL_l$ as this value will change in the equilibration if a laminate is formed. Before the time step calculations are completed, the laminate thickness will be calculated using an updated

$${}_nL_l$$

in equilibration. The value of ${}_{n-1}L_l$ will not change if no laminates branch. See section 3.4 for full details; a note is left here to maintain comprehension of the above equation.

Adding in the constraint that the children fit inside the parent

$${}_nL_l^c = \begin{cases} \textit{equation (3.25)}, & \textit{if (equation (3.25))} < {}_{n-1}L_l \\ {}_{n-1}L_l\,, & \textit{otherwise} \end{cases} \tag{3.26}$$

The previous work of Aubrey and Ortiz [10] treated the nonlocal energy as a perturbation to the total energy. This work minimizes it directly, as it is shown in section 3.3.1 that the

dislocation wall energy will eventually be comparable in magnitude to the plastic deformation energy giving a strong interaction between L_l^c and a_l.

3.3 Nonlocal Energy

Following the ideas of Aubrey and Ortiz [10], two terms of nonlocal energy will be included due to the formation of laminate structures: the dislocation wall energy and the boundary layer energy.

3.3.1 Dislocation Wall Energy

When a laminate branches into two laminates with different slip planes, a dislocation wall forms between them. The new dislocation walls impede dislocation motion and, thus, shorten the mean free path of the mobile dislocations. As derived in Aubrey and Ortiz using Orowan's relation [10], shortening the mean free path causes plastic energy for a given deformation to increase. This increase of the plastic deformation energy corresponds to an increase in critical resolved shear stress. Hence formation of dislocation walls increases the energy necessary for further plastic deformation for the individual laminate's slip system, but due to the gained freedom in active slip systems to release stored elastic energy the laminate formation may lower the global deformation energy.

Here the ideas of Aubrey and Ortiz [10] are expanded to not just using the width of the laminate as the mean free path for dislocations, but to include the angle between the path of the dislocation and the dislocation wall. This allows a first estimate of morphology in the structure to be included. The inclusion of the dislocation path geometry means finer laminates will form if the slip plane (and thus the dislocation paths) is near parallel to the dislocation wall. This change significantly lowered the boundary layer energy and often

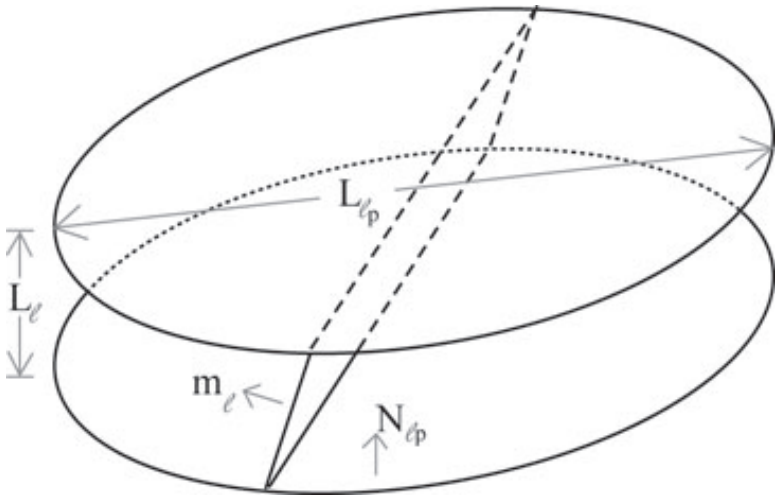

Figure 3.4. *Geometry of slip plane between two dislocation walls*

changed the lowest energy (active) system in simulations. This is particularly important for the special cases where the dislocation path normals in sibling laminate structures are identical and thus, no dislocation walls form to impede further dislocation slip [7].

For a given slip system β, dislocations are assumed to move until encountering the boundary of the laminate. Note that all dislocation paths reside on the slip plane regardless of the type of dislocation, thus one needs to consider the general case of computing the mean free path of dislocations on the slip plane of laminate l which is between two parallel dislocation walls, reference Figure 3.4. The width between the parallel dislocation walls L_l, is defined by the computation of $L^c_{l_p}$ and λ_l from equation (3.8). The length of the dislocation walls is approximated as the width of the parent laminate: L_{l_p}. Note that this approximation is a minimum, the true length may be much longer depending on the angle the parent laminate makes with its parent and grandparent and so on. This is not of concern though as a separation of scales is assumed, e.g., $L_{l_p} \gg L^c_{l_p}$. As this assumption will be used for simplification, it is not of any consequence if L_{l_p} is underestimated. The normal to the dislocation walls is $\mathbf{N}_{l_p}$ and the normal to the slip plane is $\mathbf{m}_l$.

Table 3.1. *L/A ratios for generic slip system A6*

System	**n***(not normalized)*	$\frac{L_{A6}}{A_{A6}}$
A2	$(\bar{1}11)$	0
A3	$(\bar{1}11)$	0
A6	$(\bar{1}11)$	0
B2	$(11\bar{3})$	$2\sqrt{\frac{2}{11}}$
	(211)	1
B4	(011)	$\frac{1}{\sqrt{3}}$
	$(11\bar{1})$	$\frac{2}{3}\sqrt{2}$
B5	(100)	$\sqrt{\frac{2}{3}}$
	$(00\bar{1})$	$\sqrt{\frac{2}{3}}$
C1	$(10\bar{1})$	$\frac{1}{\sqrt{3}}$
	(111)	$\frac{2}{3}\sqrt{2}$
C3	$(12\bar{1})$	1
	(113)	$2\sqrt{\frac{2}{11}}$
C5	(001)	$\sqrt{\frac{2}{3}}$
	$(0\bar{1}0)$	$\sqrt{\frac{2}{3}}$
D1	$(\bar{1}12)$	$\frac{1}{3}$
	(311)	$4\sqrt{\frac{2}{33}}$
D4	$(13\bar{1})$	$4\sqrt{\frac{2}{33}}$
	$(13\bar{1})$	$\frac{1}{3}$
D6	$\in$ plane containing m_{D6} and m_{A6}	$\in (0,1)$

The slip plane is approximated as a rectangle defined by two lengths, call the lengths A and B defined by

$$A = \frac{L_l}{\sqrt{1-(\mathbf{m}_l \cdot \mathbf{N}_{l_p})^2}} \quad , \tag{3.27}$$

$$B = L_{l_p} \quad . \tag{3.28}$$

Table 3.1 lists the ratios L/A for the slip system A6 given the sibling slip system for single slip using all possible wall normals as calculated by Ortiz and Repetto [7]. Due to symmetries of the slip systems it does not matter which system was chosen, A6 is a completely generic choice. Note microstructures involving only the same slip system (i.e., A6 and A6 in this example) are indistinguishable in this theory. The value of L/A ranges from a maximum of

1 (slip plane perpendicular to laminate wall normal) to a minimum of $\frac{1}{3}$, excluding the same slip plane laminates. The same slip plane laminates (i.e., A slip systems in this example), are parallel with the dislocation wall normal and thus do not interact with it. These are discussed in section 3.3.1.1 subsequently.

The mean free path of dislocations on the slip plane, h_l, is defined by

$$h_l \equiv \frac{\sum paths}{\#paths} \quad , \tag{3.29}$$

using $\#paths$ to mean the count of all paths. It is assumed that dislocations are generated uniformly at all locations in the plane. Noting that all dislocations (edge and screw) move in the slip plane and that various dislocations mixed between edge and screw may move in any direction to provide the appropriate slip, it is also assumed that the direction of motion of the dislocations is uniformly distributed. The number of paths can be computed

$$\#paths = \int_{\Omega} \int_{\alpha=0}^{\alpha=2\pi} d\alpha \; d\bar{x} = 2\pi AB \quad , \tag{3.30}$$

where $\bar{x}$ is the location coordinate on the slip plane and Ω is the area of the slip plane.

Define $p[\alpha, \bar{x}]$ as the path length of the dislocation starting at $\bar{x}$ and moving at the angle α. Thus,

$$\sum paths = \int_{\Omega} \int_{\alpha=0}^{\alpha=2\pi} p[\alpha, \bar{x}] d\alpha \; d\bar{x} \quad . \tag{3.31}$$

Referencing figure 3.5

$$\theta_1 = \arccos[\frac{B-x}{\sqrt{(B-x)^2+y^2}}] \quad , \tag{3.32}$$

$$\theta_2 = \arccos[\frac{B-x}{\sqrt{(B-x)^2+(A-y)^2}}] \quad , \tag{3.33}$$

$$\theta_3 = \arccos[\frac{x}{\sqrt{x^2+(A-y)^2}}] \quad , \tag{3.34}$$

$$\theta_4 = \arccos[\frac{x}{\sqrt{x^2+y^2}}] \quad , \tag{3.35}$$

$$\alpha_1 = -\theta_1 \quad , \tag{3.36}$$

$$\alpha_2 = \theta_2 \quad , \tag{3.37}$$

$$\alpha_3 = \pi - \theta_3 \quad , \tag{3.38}$$

$$\alpha_4 = \pi + \theta_4 \quad . \tag{3.39}$$

This gives

$$p[\alpha, \bar{x}] = \begin{cases} \frac{B-x}{\cos\alpha} & \textit{if } \alpha_1 \leq \alpha < \alpha_2 \quad , \\ \frac{A-y}{\sin\alpha} & \textit{if } \alpha_2 \leq \alpha < \alpha_3 \quad , \\ \frac{x}{\cos\alpha} & \textit{if } \alpha_3 \leq \alpha < \alpha_4 \quad , \\ \frac{-y}{\sin\alpha} & \textit{if } \alpha_4 \leq \alpha < \alpha_1 \quad . \end{cases} \tag{3.40}$$

$B \gg A$ allows for the small angle approximations given in table 3.2. These approxima-

Table 3.2. *Small angle approximations*

$\cos\alpha_1 \approx 1$	$\sin\frac{\alpha_1}{2} \approx -\frac{\theta_1}{2}$	$\cos\frac{\alpha_1}{2} \approx 1$	
$\cos\alpha_2 \approx 1$	$\sin\frac{\alpha_2}{2} \approx \frac{\theta_2}{2}$	$\cos\frac{\alpha_2}{2} \approx 1$	
$\cos\alpha_3 \approx -1$	$\sin\frac{\alpha_3}{2} \approx 1$	$\cos\frac{\alpha_3}{2} \approx -\frac{\theta_3}{2}$	
$\cos\alpha_4 \approx -1$	$\sin\frac{\alpha_4}{2} \approx 1$	$\cos\frac{\alpha_4}{2} \approx \frac{\theta_4}{2}$	
$\theta_1 \approx \frac{y}{B-x}$	$\theta_2 \approx \frac{A-y}{B-x}$	$\theta_3 \approx \frac{A-y}{x}$	$\theta_4 \approx \frac{y}{x}$

tions are good so long as the point $\bar{x}$ is far from the edges of length A, but that area is quite

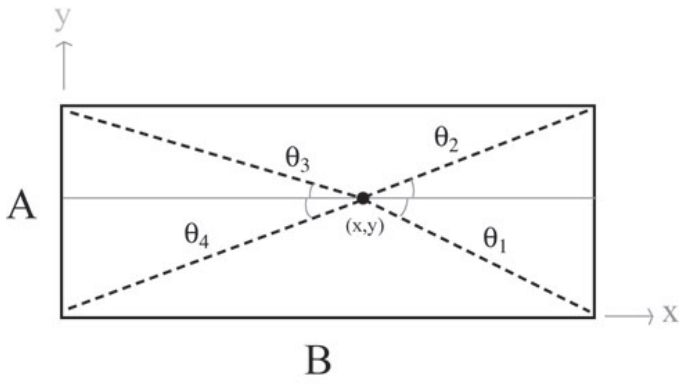

Figure 3.5. *Coordinates and angles on the slip plane*

small (again due to $B \gg A$). Integrating p over α and then applying these approximations yields

$$\begin{aligned}\int_{\alpha=0}^{2\pi} p d\alpha \approx \quad & 2A - y\left(\ln\left[-\frac{y}{4(B-x)}\right] + \ln\left[\frac{y}{x}\right]\right) \\ + \quad & (y-A)\left(\ln\left[\frac{A-y}{4(B-x)}\right] + \ln\left[\frac{y-A}{x}\right]\right) \quad . \end{aligned} \tag{3.41}$$

Then integrating over the domain of the slip plane, and taking only the real part

$$\int_{\Omega}\int_{\alpha=0}^{2\pi} p d\alpha \; d\bar{x} = A^2 B(1 + 2\ln[\frac{2B}{A}]) \tag{3.42}$$

yields the mean free path by equation (3.29)

$$h_l = \frac{A_l(1 + 2\ln[\frac{2B_l}{A_l}])}{2\pi} \quad . \tag{3.43}$$

It is desired to remove the parameter B from the computation of the mean free path as its value is not readily available. The value of h_l will be approximated as a linear function of A_l using the separation of length scales inherit in laminate structures ($B \gg A$). The value of $\zeta \equiv {}_n h_l / A_l$ is investigated. A plot of ζ vs. $\frac{B}{A}$ is given in figure 3.6. For the range

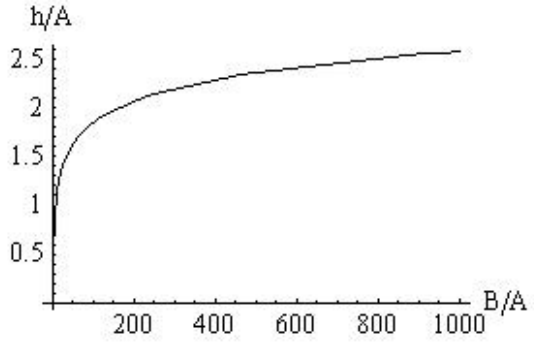

Figure 3.6. *Plot of* $\frac{h}{A}$ *vs.* $\frac{B}{A}$

$(B/A) \in [100, 1000]$, $\zeta \in [1.846, 2.579]$. Due to the small variation of ζ in a domain of reasonable values, the extra computation is warranted as excessive and the parameter ζ is approximated as a constant. For this work $\zeta_l = 2$ is chosen.

This gives a value for the dislocation mean free path

$$ {}_n h_l = \zeta_l A_l = \frac{\zeta_l \, {}_n L_l}{\sqrt{1 - (\mathbf{m}_l \cdot \mathbf{N}_{l_p})^2}} \quad , \tag{3.44} $$

and by equation (3.8)

$$ {}_n h_l = \frac{\zeta_l \lambda_l \, {}_n L^c_{l_p}}{\sqrt{1 - (\mathbf{m}_l \cdot \mathbf{N}_{l_p})^2}} \quad . \tag{3.45} $$

Note although the angle between $\mathbf{m}_l$ and $\mathbf{N}_{l_p}$ may change during plastic slip, the length A will remain constant. This is true because plastic slip is purely a shear deformation and thus will not cause the material to stretch along the shear direction. A shear deformation would cause the angle between $\mathbf{m}_l$ and $\mathbf{N}_{l_p}$ to change, but this would correspond to a change in the perpendicular length measured ${}_n L_l$ that would compensate to keep the value of A constant. Assuming elastic stretch deformation to be negligible, the mean free path calculations can thus be done in the reference (undeformed) configuration accounting only for changes in the length ${}_n L_l$ and treating $\sqrt{1 - (\mathbf{m}_l \cdot \mathbf{N}_{l_p})^2}$ as a constant.

As was derived by Aubrey and Ortiz [10] using Orowan's relation, the effect of the dislocation walls shortening the mean free path increases the critical resolved shear stress of the material:

$$ {}_n\tau_l^c = \tau_0^c + \frac{T}{b\ {}_nh_l} \quad , \tag{3.46} $$

where τ_0^c is the material-dependent initial critical resolved shear stress, T is dislocation line tension, and b is the Burgers vector. This increase of the critical resolved shear stress with refinement of the subgrain dislocation structures causes several forms of hardening in this model.

The added nonlocal energy of the dislocation wall including the increase in τ^c to both children (i.e., l is the branch in the following equation instead of a leaf) can be inferred as

$$ \begin{aligned} {}_nW_l^{DW} &= \frac{T}{b}\left(\frac{{}_n\gamma_{l^-}\lambda_{l^-}}{{}_nh_{l^-}} + \frac{{}_n\gamma_{l^+}\lambda_{l^+}}{{}_nh_{l^+}}\right) \\ &= \frac{T}{b\ {}_nL_l^c}\left(\frac{{}_n\gamma_{l^-}}{\zeta_{l^-}}\sqrt{1-(\mathbf{m}_{l^-}\cdot\mathbf{N}_l)^2} + \frac{{}_n\gamma_{l^+}}{\zeta_{l^+}}\sqrt{1-(\mathbf{m}_{l^+}\cdot\mathbf{N}_l)^2}\right) \quad . \end{aligned} \tag{3.47} $$

To obtain the equations that are in Aubrey and Ortiz [10], apply the conversion $h_{l^\pm} \rightarrow L_{l^\pm}$ and assume $(\mathbf{m}_{l^\pm}\cdot\mathbf{N}_l) = 0$.

The dislocation wall energy is in general not a perturbation of the total plastic deformation energy, as can be seen by an estimation of values for a single leaf l at time n. Previous work has treated it as a perturbation [10]. The plastic energy is ${}_nW_l^p = ({}_n\tau_l^c)({}_n\gamma_l)$, while the dislocation wall energy is ${}_nW_l^{DW} = \frac{T({}_n\gamma_l)}{b({}_nh_l)}$. Thus,

$$ \frac{{}_NW_l^p}{{}_nW_l^{DW}} = \frac{b({}_nh_l)({}_n\tau_l^c)}{T} \quad . \tag{3.48} $$

Generally for metallic materials the order of $T \approx 10^{-10}$ N, $b \approx 10^{-10}$ m, and $\tau \approx 10^6$ N/m^2;

yielding $\frac{W_l^p}{W_l^{BL}} \approx h_l * 10^6$ 1/m. Using these estimates, only for laminates larger than approximately 10^{-4} m may W^{DW} be treated as a perturbation; although, any laminate this large should find forming finer laminates energetically favorable and eventually invalidate this assumption. Thus, the dislocation wall energy, W^{DW}, is never treated as a perturbation in this work.

3.3.1.1 Laminates with Coplanar Slip

The special case of branched laminates with active coplanar slip systems have the children's slip planes parallel to the dislocation wall predicted to form between the children. In this case, the two children's dislocations move in parallel directions and no dislocation wall forms [7]. Note in this model, once the angle of the slip plane to the wall normal is taken into account, $h_l \to \infty$, appropriately giving a dislocation wall energy of zero. If there is no dislocation wall energy, the laminate will be able to form at an infinitesimal width and negate any boundary layer energy as well. This gives a total nonlocal energy of zero, meaning branches with identical slip planes on either side are zero energy structures. Zero-energy structures are obviously problematic. In reality, the value of h_l for two coplanar laminates should be the length of the parent structure containing them.

There is a second problem with coplanar laminates. If no dislocation walls form, then there is nothing to prevent the dislocations in the children of the coplanar laminate from slipping across these boundaries, and thus forming at the length scale of the parent. As this change in length scale is not accounted for in the theory, the children of laminates with coplanar siblings would form at lower length scales and thus harden too much. The two problems caused by the lack of dislocation walls is the reason a coplanar slip approach is needed and was already discussed in section 2.3.4.

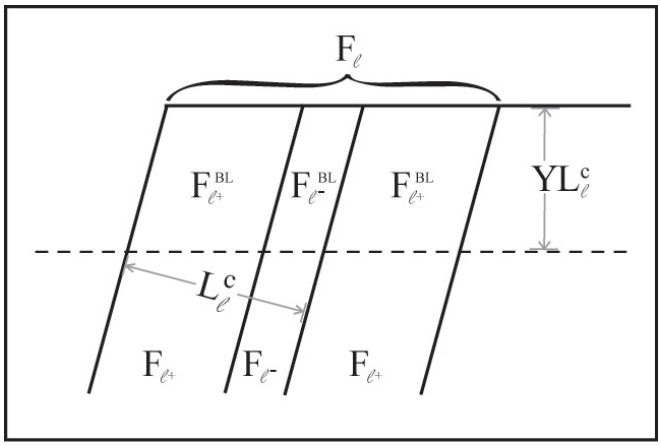

Figure 3.7. *Detailed figure showing boundary layer variables*

Although these coplanar systems should not only self harden but harden each other [2], the results of Franciosi [26] and analysis of Bronkhorst [23] and Havner [24] suggest coplanar slip systems should exhibit much less latent hardening than other systems. This work treats coplanar systems as mutually self hardening (i.e., the slip on two active coplanar slip systems is added and treated as a single slip system which self hardens). This differs from traditional multislip theories in which the hardening of these systems is often approximated identical to all other systems [16, 15].

3.3.2 Boundary Layer Energy

The boundary layer energy is computed from the elastic deformation that maps the underlying parent material to the two children's deformations. By referencing figure 3.7 note that the outside wall of the laminate is at the parent's deformation, ${}_n\mathbf{F}_l$, while the bulk volume of the children are at their respective deformations, ${}_n\mathbf{F}_{l^\pm}$. The boundary layer's state of deformation must transition from the parent deformation to the child's deformation. A linear

transition is assumed giving the average deformation of the boundary layer as

$$ {}_n\mathbf{F}^{BL}_{l^{\pm}} = \frac{1}{2}({}_n\mathbf{F}_l + {}_n\mathbf{F}_{l^{\pm}}) \quad . \tag{3.49} $$

Taking the boundary layer deformation to be elastic yields an energy for the boundary layer

$$ {}_nW^{BL}_l = \lambda_{l^+}\left(W^e[(\mathbf{F}^{BL}_{l^+})({}_n\mathbf{F}_l)^{-1}] - {}_nW_{l^+}\right) + \lambda_{l^-}\left(W^e[(\mathbf{F}^{BL}_{l^-})({}_n\mathbf{F}_l)^{-1}] - {}_nW_{l^-}\right) \quad , \tag{3.50} $$

where the terms ${}_nW_{l^{\pm}}$ are subtracted as a correction to the total energy since the energy of the boundary layer volume was assumed to have the child's deformation in previous calculations. Note the boundary layer energies will remain positive as the energy of the child deformation subtracted involves a low energy plastic deformation, while the energy of the boundary layer is elastic in nature. Recall the definition of ${}_nW_{l^{\pm}}$ is the plastic and elastic energy in the individual leaf and does not include the previous plastic deformation in laminate l and other ancestors of the leaf; thus, the value of W^{BL}_l is actually the difference between the energy in the boundary layer volume and the average bulk deformation energy of the branched laminate. It acts as an energy penalty.

The formulation given here differs from the work of Aubrey and Ortiz [10] in the correction of the additional elastic deformation to be $(\mathbf{F}^{BL}_{l^+})({}_n\mathbf{F}_l)^{-1}$ rather than $(\mathbf{F}^{BL}_{l^+})$ only. This change is due to the boundary layer accommodating the deformation from the initial parent material to the child's deformation rather than from an initial undeformed state to the child's deformation.

Note that this is an energy density for the boundary layer, and as such must be added only for the portion of material which is in the boundary layer. The contribution to the total

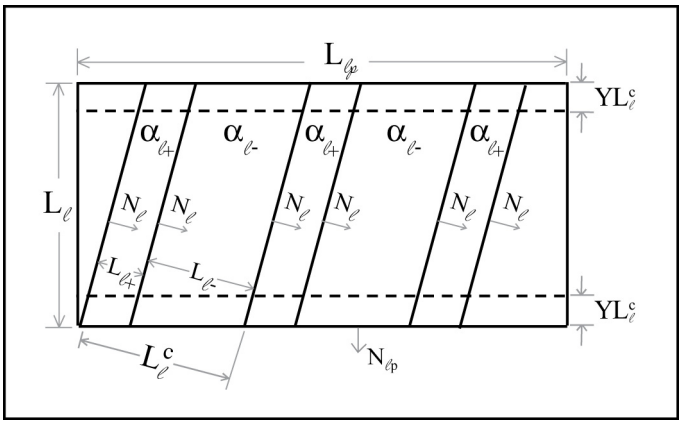

Figure 3.8. *Calculation of the boundary layer volume. Illustration not to scale.*

energy density is scaled by the fraction of the boundary volume to the total volume of the simple laminate. Reference figure 3.8, assuming the dislocation wall parallel to N_{l_p} is circular, the total volume of one layer of the branched laminate L_l is $\frac{\pi}{2} L_l L_{l_p}^2$. The corresponding boundary area is $\pi L_{l_p}^2$, neglecting the small contribution $2\pi L_l L_{l_p}$ justified by $L_{l_p} \gg L_l$. Note the geometric assumption of a circular area cancels in the ratio of the total volume to volume of boundary layer, and thus the geometric assumption of circular domain has little influence on this calculation. Taking the combined children's laminate lengths, $L_l^c = L_{l^+} + L_{l^-}$, the total nonlocal energy density scales as

$$W_l^{NL} = W_l^{DW} + 2\Upsilon \frac{L_l^c}{L_l} W_l^{BL} \quad , \tag{3.51}$$

where Υ is a scaling factor determining the depth the boundary layer penetrates in the laminate in multiples of L^c.

In the work of Ortiz, Repetto, and Stainier [9] showing boundary layers composed of refining laminate structures, the boundary layer penetration is on the order of L_c. Thus, it can be assumed Υ should be somewhere on the order of 1. Aubrey and Ortiz [10] indirectly assign Υ as $\frac{1}{2}$.

As the boundary layer term is scaled by $\frac{L_l^c}{L_l}$ and it is assumed $L_l^c \ll L_l$, the boundary layer contribution to the total energy can be assumed small. Due to the minimal contribution, it appears justified to treat it as a perturbation when solving for $\mathbf{a}$.

3.4 Equilibration Updates

As the macroscopic deformation, ${}_n\mathbf{F}$, increments with each time step, it is necessary to update the values of the polarization vectors, ${}_n\mathbf{a}_l$, in order to keep the stress compatible across the dislocation walls. The values of the laminate thicknesses, ${}_nL_l^c$, are also updated as it provides a hardening behavior, and mathematically the thickness depends on variables that are being updated, ${}_nW_l^{BL}$ and ${}_n\gamma_l$. If the thicknesses were not updated, but rather formed at a single step and held constant afterward, the values of the thicknesses would depend on such things as step size. This is not a desired behavior.

It is desirable to allow multiple rank structures to form within the same time step, e.g., a leaf may branch into two children, then at the same time step those children may further branch into children and so on. This feature was added into the theory in this work, previous works allowed only for one branching step to occur at each deformation step. The addition of equilibrating the laminate thicknesses for the entire structure described in this section allows multiple branches to form in the same time step. If the thicknesses are not equilibrated as an entire structure, having a laminate with $\gamma = 0$, would cause instabilities with W^{BL} when computing thickness for the children of this laminate. When multiple rank branches form at the same time step, the $\gamma = 0$ parents with no plastic deformation themselves essentially become space holders for the children.

It should be noted that a complete optimization of the laminate structure would require the equilibration be done simultaneously with the formation of new branches. Essentially,

when checking if a new branch forms the structure should be equilibrated, as well as checking every possible combination of other new branches in the tree and equilibrating each combination. Obviously, this problem quickly becomes non-tractable. To avoid this the structure from the previous time step is equilibrated at the beginning of each deformation step for the new deformation gradient, ${}_n\mathbf{F}$, and then each leaf is checked individually to see if it branches. This process of equilibration and branching is repeated until no new leaves form.

To remove elastic leaves, a minimum limit should be set on the slip strain, γ_l, for a branch to form. Without this restriction leaves may form which after equilibration, only deform elastically. Since the laminates in this theory are based on the formation of subgrain dislocation structures, if a leaf is only reacting elastically, it should not have been formed. To avoid dependence on the size of the time steps, a small numerical restriction of $\gamma_l \geq 1*10^{-14}$ is chosen. This restriction is small enough to remove only leaves with energy benefits on the order of computational error. Elastic leaves did not form in any of the simulations presented in this paper.

From this point on, the subscript designating step discretization n will be left off. As the following calculations in this section show the equilibration for a single time step, it is understood all values have the same n. The reader is referred to previous sections for an understanding of which values are changing over time steps.

3.4.1 Compatibility of Stress and Evolution of the Polarization Vector

As each new macroscopic deformation step, $\mathbf{F}$, is introduced, the equilibration of the stresses across the dislocation walls needs to be updated. Equation (3.22) must be satisfied for each branch simultaneously. The value of the deformation jump $\mathbf{a}$ is recomputed for branches in the microstructure using the new global $\mathbf{F}$. This was shown and implemented by Ortiz,

Repetto, and Stainier [9]. Note that only the leaves in the microstructure are active and free to evolve new values of slip strain γ, so only the leaves obtain new slip strain values to accomplish this equilibration.

Noting the optimization of the deformation jump, $\mathbf{a}_l$, and the laminate thicknesses, $\mathbf{L}_l^c$, are interrelated, an iteration similar to that used in solving for individual branches is used. The $\mathbf{a}_l$ are solved for using the previous values of $\mathbf{L}_l^c$, after which $\mathbf{L}_l^c$ is optimized for the new values of $\mathbf{a}_l$. This is repeated until the change in $\mathbf{L}_l^c$ reaches a specified tolerance.

3.4.2 Evolution of Laminate Thickness

Previously, the method for obtaining the optimal laminate thickness when a single laminate bifurcates into two laminates was given (cf. section 3.2.5). This section deals with optimizing the thicknesses of an entire laminate microstructure. This is done as part of equilibration.

3.4.2.1 Laminate Evolution

In this theory, the dislocation walls form at an instant, whereas in real materials the dislocation wall will form slowly as more dislocations entangle and form dislocation walls. The evolution of the thickness over time is considered to approximate the formation of the walls over time and refinement of the length scale as new dislocations form between existing dislocation walls.

If the laminates are formed and not updated, the thickness of the laminates is dependent upon the deformation step size because the values used to calculate the thickness (W^{BL} and γ) evolve through the deformation steps. Branching occurs when the energy of the laminate deformation mechanism is less than the energy of a single slip deformation, but due to discretization of deformation steps, the magnitude where these two energies are equal is

generally overshot. The evolution of the thicknesses allows for a value to be converged on with further deformation and provides a self hardening behavior.

The laminate thickness should have changes not just in the leaves but also in the entire tree structure. This is particularly true if more than one layer of laminate is to form within the same time step. Previous laminate theories to date have only allowed one layer of laminate to form at each time step, thus restricting the reasonable magnitude of deformation step that can be taken. Under this theory, it is possible to form any rank of laminate where only the leaves have non-zero slip strain, γ. A $\gamma = 0$ branch is essentially a place holder for the volume of its descendants. It is also assumed that the dislocation walls of previous branches which have further branched have a degree of mobility. At this time no limits to the mobility of the dislocation walls is used, the length is based on energy optimization.

The minimization of the nonlocal energy with respect to all L_l^c is

$$\min_{\{L_l^c|\ l=1,\ldots,Z\}} \sum_{l'=1}^{Z} W_{l'}^{NL} \quad , \tag{3.52}$$

where Z is the number of laminates in the microstructure. Noting that the only lengths that influence the nonlocal energy of a particular laminate l are L_l^c and $L_{l_p}^c$ (see equation (3.24)), the minimization of the total nonlocal energy with respect to a specific L_l^c is

$$\frac{\partial \sum_{l'=1}^{Z} W_{l'}^{NL}}{\partial L_l^c} = \frac{\partial W_{l^-}^{NL}}{\partial L_l^c} + \frac{\partial W_{l^+}^{NL}}{\partial L_l^c} + \frac{\partial W_l^{NL}}{\partial L_l^c} = 0 \quad , \tag{3.53}$$

which yields

$$L_l^c = \sqrt{\left(\frac{L_{l^+}^c W_{l^+}^{BL}}{\lambda_{l^+}} + \frac{L_{l^-}^c W_{l^-}^{BL}}{\lambda_{l^-}} + \frac{\delta_l}{2\Upsilon} \right) \frac{\lambda_l}{W_l^{BL}} L_{l_p}^c} \quad , \tag{3.54}$$

where use has been made of equation (3.8): $L_l = \lambda_l L^c_{l_p}$ and

$$\delta_l \equiv \frac{T}{b}\left(\frac{\gamma_{l^+}}{\zeta_{l^+}}\sqrt{1-(m_{l^-}\cdot N_l)^2}+\frac{\gamma_{l^-}}{\zeta_{l^-}}\sqrt{1-(m_{l^-}\cdot N_l)^2}\right) \quad . \tag{3.55}$$

Note that each L_l depends on its parent and children, thus each parent depends on each of its descendant's lengths and each child's length also depends on each of its ancestor's lengths. This infinite loop of dependencies is overcome by starting with the known length of the rank 0 laminate, L_0, which is a required input. As an initial starting condition, set $L^c_0 = L_0$ and $\lambda_0 = 1$, then a direct iteration by decreasing rank of the structure is possible.

To avoid ambiguity in the above calculations, if $l^{\pm}$ is a leaf, $W^{BL}_{l^{\pm}} = 0$. Note in this case equation (3.25) is returned.

3.4.2.2 Hardening

Both traditional mechanisms of hardening, self hardening and latent hardening, are reproduced by the laminate size evolution. As the slip strain within a laminate increases with deformation, the boundary layer energy increases. The simplest approximation for the boundary layer energy density is $W^{BL} = \mu\gamma^2$, where μ is the shear modulus. Considering equation (3.25), the laminate size will decrease with increasing strain. Due to equation (3.46) this causes a form of self hardening. When a new slip system is activated, the material must branch, and thus both the new laminate and the existing one will decrease in size, causing a form of latent hardening.

It is also interesting to note that the magnitude of latent hardening is dependent upon the systems that are activated. The changes in magnitude of hardening are caused by the variance in the mean free path of the systems (cf. table 3.1). The results of the mean free

path calculations display a similar relationship for coplanar, colinear, and other forms of hardening in multiple slip as described by Franciosi and Zauoi [2] and Havner [24].

3.5 Stress Jumps on Laminate Formation

It is shown that when a laminate forms there is a discontinuity in the stress state. This is important as any finite element method generally uses iterative solutions to apply traction boundary conditions and to obtain equilibration between elements. A discontinuity in the stress may cause the iterative changes in the deformation gradient used to obtain a specified traction to fail to converge. Although this can happen in more dimensions and was often observed in two, the concept can be illustrated simply in onedimension, see figure 3.9.

If the target value P^* falls in the stress discontinuity, when the point F_1 is reached the derivative $\frac{\partial P}{\partial F}$ of microstructure 1 will provide the new input value F_2, which in turn will provide F_1. This cycle occurs if P^* falls anywhere between $P[F_1]$ and $P[F_2]$. This illustration is a simplification for demonstration only; the derivative $\frac{\partial P}{\partial F}$ is not constant for a given microstructure, nor generally are the traction boundary conditions only applied to one component of the nine-component tensor.

The stress discontinuity must be eliminated to guarantee convergence of applied traction boundary conditions. As they are due to oscillations between two or more microstructures, the solution is to prescribe a single microstructure. With only one prescribed microstructure, there are no discontinuities in the stress, and the traction boundary conditions can be met by iteration. The proper criteria for selecting which microstructure should be used is debatable. An obvious choice would be to select the least developed microstructure, thus allowing the material to select a more complicated microstructure at the next deformation step, but this requires tracking and storing all microstructures that occur. Another option would be to

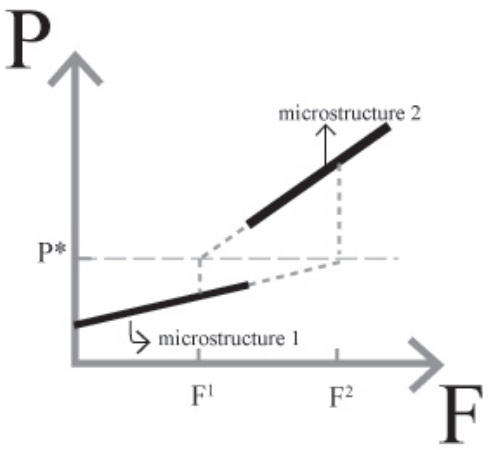

Figure 3.9. *Illustration of lack of convergence from a stress jump*

investigate the energy of fixing each possible microstructure and selecting the lowest. This would involve long computations for many structures.

Since it is also difficult to detect when an oscillation between microstructures has occurred, this work uses an efficient random selection of microstructure. When convergence to a traction boundary condition fails after a given number of iterations, the microstructure is prescribed as the last microstructure developed. The deformation is then equilibrated with only this microstructure. Note the deformation is still evolved, but the microstructure and slip systems are fixed.

The following shows the magnitude of the minimum jump in stress. The calculations are purely academic as it would be easier to compute the jump directly, but this proves the existence of the jump and gives the starting point for the possibility of removing the jump in later work.

The energy of laminate l deforming by single slip is

$$W_l^{ss} = W_l^e + W_l^p = W_l^e + \tau_l^c \, {}_{n+1}\gamma_l \quad . \tag{3.56}$$

The energy of the laminate l branching and forming the two laminates l^+ and l^- is

$$W_l^{lam} = \lambda_{l^+} W_{l^+}^{ss} + \lambda_{l^-} W_{l^-}^{ss} + \tau_l^c \ {}_n\gamma_l + \frac{2\Upsilon L_l^c}{L_l} W_l^{BL} \quad . \tag{3.57}$$

A laminate forms when the energy of single slip is equal to the energy of the laminate (not accounting for discrete time steps)

$$W_l^{ss} = W_l^{lam} \quad . \tag{3.58}$$

Taking the derivative of this equality with respect to $\mathbf{F}$

$$\begin{aligned} \frac{\partial W_l^{ss}}{\partial \mathbf{F}} &= \frac{\partial W_l^{lam}}{\partial \mathbf{F}} \\ &= \lambda_{l^+} \frac{\partial W_{l^+}}{\partial \mathbf{F}} + \lambda_{l^-} \frac{\partial W_{l^-}}{\partial \mathbf{F}} + \frac{2\Upsilon L_l^c}{L_l} \frac{\partial W_l^{BL}}{\partial \mathbf{F}} \quad . \end{aligned} \tag{3.59}$$

Using equation (2.2) for the stress

$$\mathbf{P}_l^{ss} = \lambda_{l^+} \mathbf{P}_{l^+}^{lam} + \lambda_{l^-} \mathbf{P}_{l^-}^{lam} + \frac{2\Upsilon L_l^c}{L_l} \frac{\partial W_l^{BL}}{\partial \mathbf{F}} \quad . \tag{3.60}$$

Noting from equation (3.5) the average stress of the laminate yields

$$\mathbf{P}_l^{ss} - \mathbf{P}_l^{lam} = \frac{2\Upsilon L_l^c}{L_l} \frac{\partial W_l^{BL}}{\partial \mathbf{F}} \quad . \tag{3.61}$$

The value of $\frac{\partial W_l^{BL}}{\partial \mathbf{F}}$ can be further evaluated for dependence on $\lambda, \mathbf{F}, \mathbf{a}$, and $\mathbf{N}$.

Chapter 4

Results and Discussion

Validation of this theory is accomplished by comparison to single crystal tests on copper. Material constants are given in section 4.1. Note these property values are taken from published experimental data and are not fit. Simulations of the theory using a single copper material point and these constants are compared against various crystal alignment tension tests. It is found that the stress response of the symmetric microstructure orientations can be captured (i.e., orientations 001, 101, and 102). The activated slip systems are compared to previous single crystal models. The affects of grain size and shape on the deformation response are also presented.

4.1 Material Properties of Copper

A significant feature of the laminate subgrain model is the small number of material constants required by the model, all of which are obtained directly from independent experimental data rather than from numerical fitting. The material constants used for the copper simulations along with references are listed in table 4.1.

Table 4.1. *Copper material constants*

Constant	**Value**	**Ref.**
Elastic Const. (C_{11})	168.4 GPa	[27]
Elastic Const. (C_{12})	121.4 GPa	[27]
Elastic Const. (C_{44})	75.4 GPa	[27]
Crit. Shear Stress (τ^c)	1.0 MPa	[28]
Burgers Vector (b)	$2.56 * 10^{-10}$ m	[29]
Line Tension (T)	$18.3 * 10^{-10}$ N	[29]

Dislocation line tension, T, is approximated using the method given in Kocks et al. [29]:

$$\begin{aligned} T_{screw} &\approx \frac{\mu b^2}{2} \quad , \\ \frac{T_{edge}}{T_{screw}} &= 1.76 \quad , \\ T &= \sqrt{T_{screw} T_{edge}} \quad , \end{aligned}$$

where T_{screw}, T_{edge} are the line tension for a screw and edge dislocation and μ is the shear modulus given in Kocks et al. [29] as 42.1 GPa.

The width of the boundary layer in units of L^c, Υ, is set to 1/2 for these simulations. This is the same value as used in Aubrey and Ortiz [10].

The initial size of the single crystal specimens used in the experiments of Franciosi and Zaoui [26, 2] is not known for model validation. As the size directly affects the hardening behavior, the sizes are approximated based upon the stress-strain data. Further details are given in the discussion.

4.2 Copper Single Crystal Simulations

Validation of the stress response of copper single crystals can be accomplished by comparison to the experimental data of Franciosi and Zaoui [26, 2]. Unfortunately, the first reference

cites the second as the source of the test data given, but the data does not appear in the second reference. This leaves some speculation on how the tests were conducted. Franciosi [26] states single crystal copper specimens were tested; each with a different crystal direction aligned to the tensile axis. The crystal directions were [001], [101], [102], [111], [112], [122], and [135].

The simulated stress normal to the tensile axis and that measured experimentally for selected orientations is presented. The evolution of the subgrain dislocation structure is also shown. A consistent deformation step of 10^{-3} is used for all simulations. All deformations with this model are assumed quasistatic as no rate dependencies are incorporated yet. Discussion of the salient structure formed and comparison of these tests follows. Afterward, the same test conditions are employed to make comparisons of grain size effects against a traditional Hall-Petch effect and to demonstrate the affect of grain shape.

4.2.1 Boundary Conditions

The boundary conditions employed cannot be taken directly from publications. Following the assumption of fixed grips seems to produce appropriate results. Note that for single crystals the choice of boundary conditions is paramount, as the deformation response is far from axisymmetric.

With nine components in the deformation gradient, $\mathbf{F}$, and nine components in the stress, $\mathbf{P}$, each component must either be specified as a displacement boundary condition (for components of $\mathbf{F}$) or as a traction boundary condition (for components of $\mathbf{P}$). Figure 4.1 gives a coordinate system and visualization for the grips. Since the test is uniaxial, F_{33} is specified as an input. $P_{11} = 0$ and $P_{22} = 0$ as these surfaces are free with no applied forces. P_{33} is the output to be solved. Additionally, it was assumed that the bottom grip

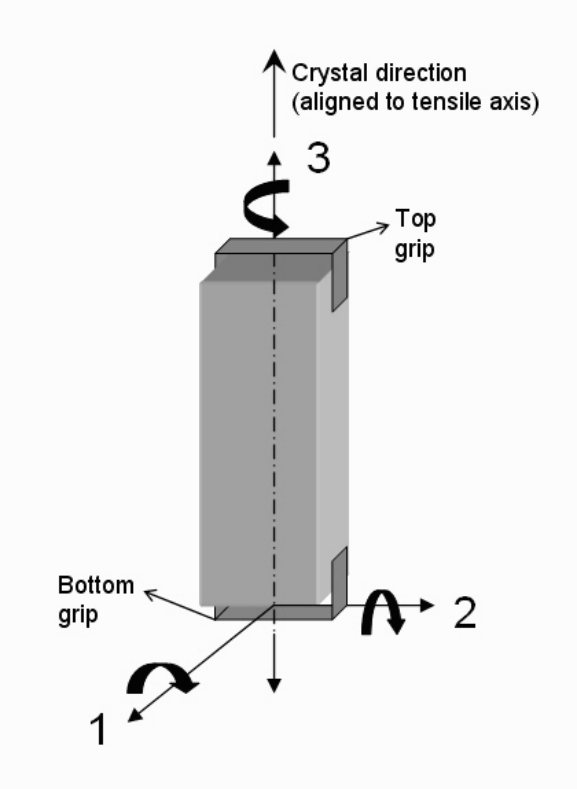

Figure 4.1. *Coordinates of fixed grip orientation for tensile Cu specimens*

did not move, and the top grip moved only in the 3 direction with no displacement in the 1 or 2 directions.

Obviously, if confined in the grips the material cannot rotate about the 1 or 2 axes. Additionally assuming the grips do not move in these directions, it follows that

$$\mathbf{F}[0,0,1]^T = [0,0,F_{33}]^T \Rightarrow F_{13} = F_{23} = 0 \quad . \tag{4.1}$$

Next, assume the material does not slip within the grips in the 3 direction, yielding

$$\mathbf{F}[1,0,0]^T = [F_{11},F_{21},0]^T \Rightarrow F_{31} = 0 \quad , \tag{4.2}$$

and

$$\mathbf{F}[0,1,0]^T = [F_{12}, F_{22}, 0]^T \Rightarrow F_{32} = 0 \quad . \tag{4.3}$$

Next, assume the fixed grips do not rotate about the 3 axis, yielding

$$\mathbf{F}[1,0,0]^T = [F_{11}, 0, 0]^T \Rightarrow F_{21} = 0 \quad , \tag{4.4}$$

and

$$\mathbf{F}[0,1,0]^T = [0, F_{22}, 0]^T \Rightarrow F_{12} = 0 \quad . \tag{4.5}$$

This gives final boundary conditions of

$$\mathbf{F} = \begin{pmatrix} F_{11} & 0 & 0 \\ 0 & F_{22} & 0 \\ 0 & 0 & F_{33} \end{pmatrix} \quad , \tag{4.6}$$

$$\mathbf{P} = \begin{pmatrix} 0 & P_{12} & P_{13} \\ P_{21} & 0 & P_{23} \\ P_{31} & P_{32} & P_{33} \end{pmatrix} \quad , \tag{4.7}$$

where non-zero values are either an input (F_{33}) or are to be solved; directly from the material model if a component of $\mathbf{P}$, or if an $\mathbf{F}$ component, through iteration to get the specified $\mathbf{P}$ component as is typical in finite element calculations.

It should be noted that these conditions leave the possibility for significant shear stresses to form. These shear stresses would be supported by the grips. The shear stress components would not have been measured.

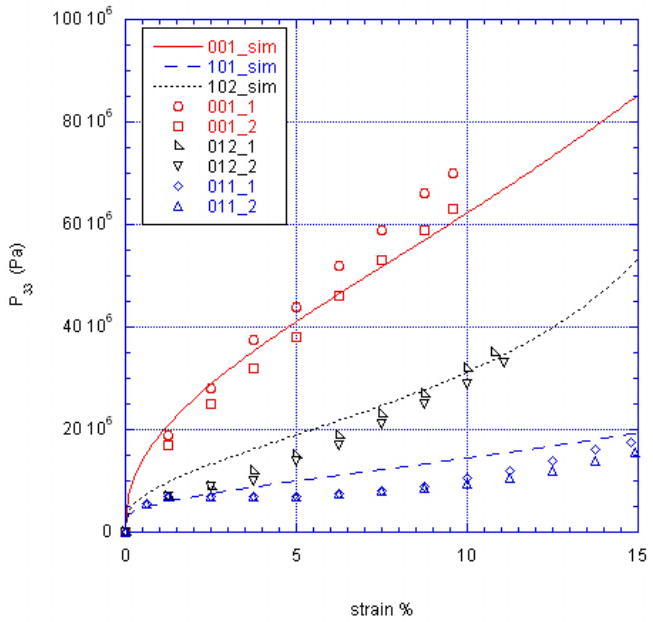

Figure 4.2. *Comparison of experimental and simulation data for single crystal copper*

4.2.2 Copper Single Crystal Validation

Figure 4.2 shows a comparison between simulated and experimental stress-strain curves for copper single crystals. Three different crystal alignments are shown: [001], [101], and [102]. The crystal direction is aligned to the tensile axis. The single points are the experimental data from Franciosi [26]; the lines are computer simulations using the laminate hardening model. Note that there are two sets of experimental data for each crystal orientation. The simulations provide good validation for the hardening mechanisms of the model for these highly symmetric crystal orientations.

Unfortunately, the size of the samples is not known. Knowing the size and orientation of each sample would define the initial grain size parameter in the simulations. As they are unknown; the sizes are adjusted to resemble the experimental data. Sizes used for

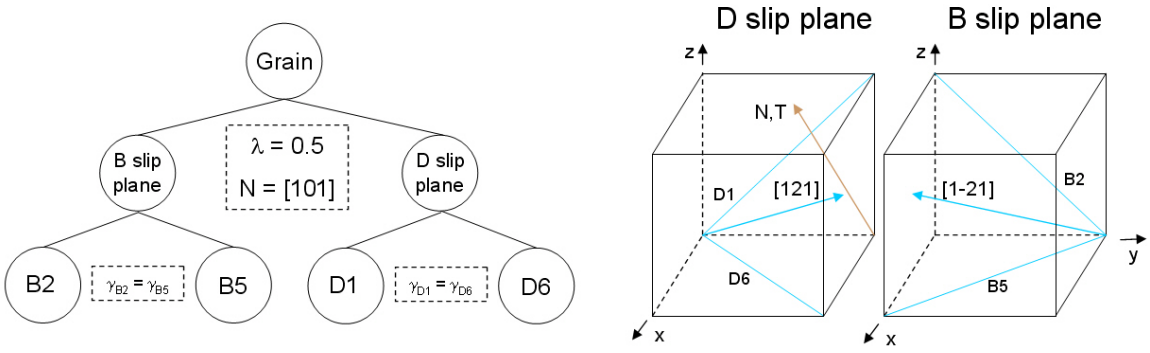

Figure 4.3. *Subgrain structure of [101] orientation simulation showing activated slip planes, wall normal, tensile direction, and effective slip directions*

the numerical samples are: [001], 0.1 mm; [101], 3.0 mm; [102], 0.5 mm. This size is the initial length perpendicular to the dislocation wall formed and not the sample diameter, and thus could vary by sample even if the sample shapes are identical. Although this amount of variation on the samples is reasonable for an experimental setup, it is also important to note that the initial grain size parameter and the boundary layer energy are coupled. From equation (3.25), the length scale of the rank one laminates varies as $\sqrt{\frac{L_o}{\Upsilon W^{BL}}}$. Hence doubling the boundary layer energy depth or magnitude is equivalent to halving the initial grain size, and so forth. In conclusion, although the initial grain size has been varied in the single crystal simulations, it is equivalent to varying the boundary layer. It would not be unreasonable that different subgrain structures would have varying boundary energy depths, i.e., varying Υ. These two unknowns are thus coupled. The number of slip systems activated (for example, by changes in the assumed boundary conditions) would also affect these results.

The subgrain structure formed during the [101] simulation and the active slip systems in the crystallographic coordinates is given in figure 4.3. The [101] orientation forms a simple laminate involving the B2 and B5 slip systems and the D1 and D6 slip systems.

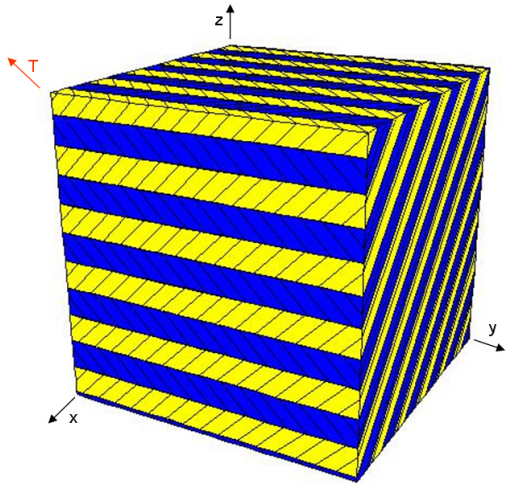

Figure 4.4. *Visualization of [101] simulation subgrain microstructure*

The dislocation wall normal, N, is parallel to the tensile axis, T, meaning the laminates form perpendicular to the tensile direction. A visualization of this structure in the crystal coordinates is given in figure 4.4 with color representing the regions in which the two different slip planes are active. The black planes within the colored regions show the orientation of the active slip plane. The tensile axis, T, is included for reference.

All four active slip systems have the same strain level as seen in figure 4.5. The stress state of the sample has no shear stresses that would provide driving force for activation of further slip systems. The only non-zero stress in the simulation is the P_{33} component.

Calculation of the Schmidt factor for the [101] orientation confirms the four predicted slip systems have the highest Schmidt factor ($\frac{\sqrt{6}}{6}$) and should activate first. This is in agreement with the work of Kalidindi and Anand [30], in which a traditional single crystal model was compared to a [101] copper single crystal deformed in compression. They also predicted the same four slip systems would activate with equal strains. The deformation involves a shortening of the 2 direction, while the 3 direction is elongated, and the 1 direction does not change. This same pattern of deformation is also seen in the work of Kalidindi and

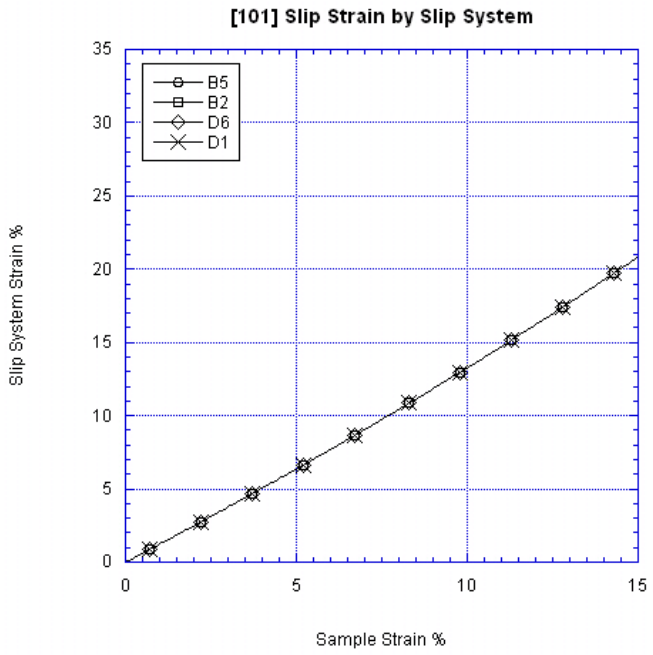

Figure 4.5. *Slip strain on active slip systems for [101] simulation*

Anand [30] with the experimental copper [101]-oriented compression sample. The trends are reversed due to the sample being in compression instead of tension (i.e, the 2 direction lengthens, while the 3 direction is compressed, and the 1 direction does not change in length). The agreement with deformed shape provides further evidence that the slip systems are correctly predicted. The stress response, activated slip planes, and deformed shape are in excellent agreement with experimental data.

The subgrain structure formed during the [102] simulation is given in figure 4.6. The [102] orientation forms the same simple laminate involving the B slip plane and the D slip plane as orientation [101], but a different wall normal. A visualization of the structure is given in figure 4.7.

The stress state of the sample has high P_{13} shear stresses that may provide driving force for activation of further slip systems, but none were activated at the 15% strain level of

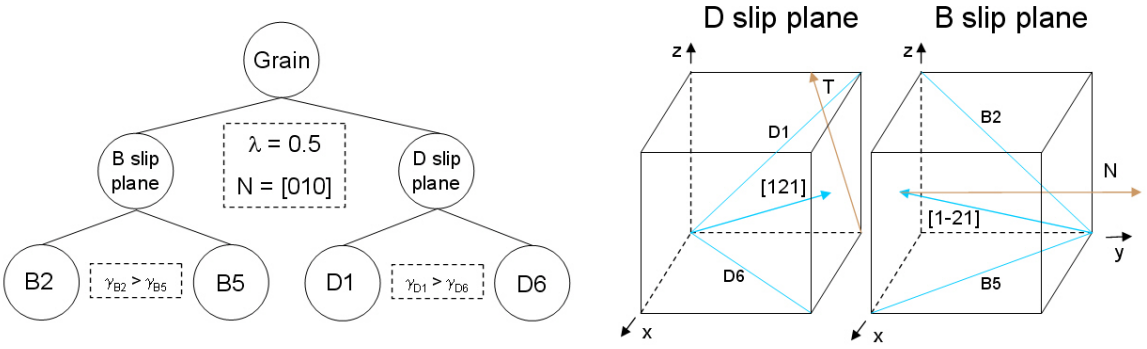

Figure 4.6. *Subgrain structure of [102] orientation simulation showing activated slip planes, wall normal, tensile direction, and effective slip directions*

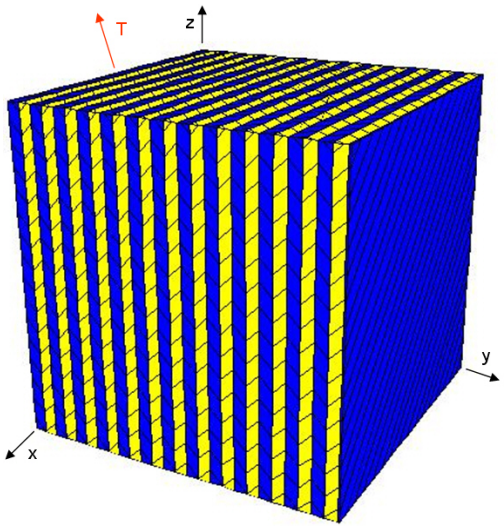

Figure 4.7. *Visualization of [102] simulation subgrain microstructure*

the simulations. Note from the plots of the activated slip strain, figure 4.8 and 4.5, that although [101] and [102] activate the same slip systems, all slip systems do not have the same slip strain in the [102] simulation.

The highest Schmidt factors for the [102] orientation are $\sqrt{\frac{6}{25}}$ for systems B2 and D1. The second highest are systems A3, B4, B5, C3, D4, and D6 at $\sqrt{\frac{3}{50}}$. This would match the prediction from the laminate model that slip systems B2 and D1 have the highest slip strain. The systems B5 and D6 are oriented to relieve the stresses that are not aligned for the simple

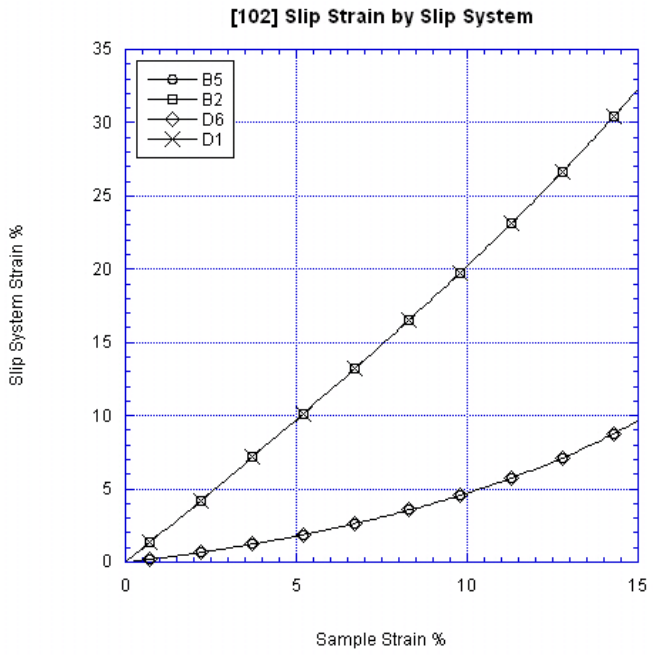

Figure 4.8. *Slip strain on active slip systems for [102] simulation*

shear on the B2 and D1 systems. No published data from traditional models is available for comparison. The stress-strain output is in excellent agreement with experimental data.

The [001] oriented sample activated the slip systems B2, B4, C1, and C3 with identical amounts of slip strain on each system activated as seen in figures 4.9 and 4.11. Note the [001] simulation activated slip on only one set of two slip planes, namely B and C, but there is an equivalent second set of slip planes, A and D. The fact that only one set of slip planes is activated means that activating all four slip planes is a higher energy configuration. The [001] orientation exhibits no shear stresses, as the [101] sample, the only non-zero stress component is P_{33}.

The highest Schmidt factor for the [001] orientation is $\frac{\sqrt{6}}{6}$ on systems A2, A3, B2, B4, C1, C3, D1, and D4. The traditional model of Cuitino and Ortiz [15] predicts that all eight systems would activate to the same slip strain. If the deformed shape of the sample were

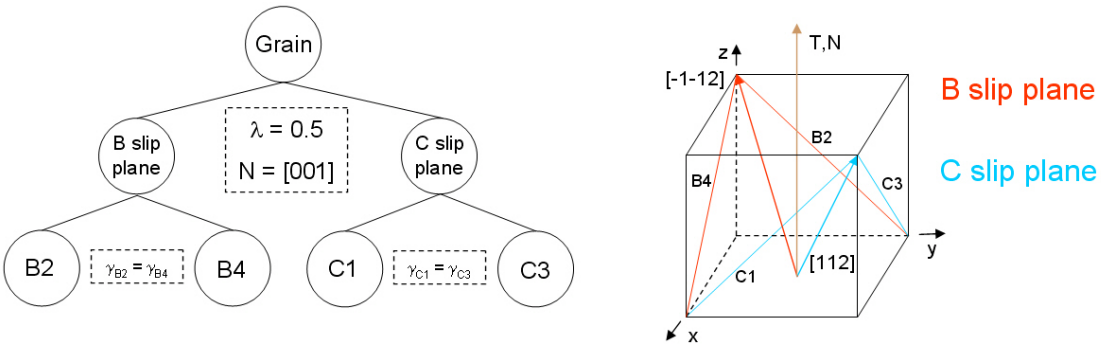

Figure 4.9. *Subgrain structure of [001] orientation simulation showing activated slip planes, wall normal, tensile direction, and effective slip directions*

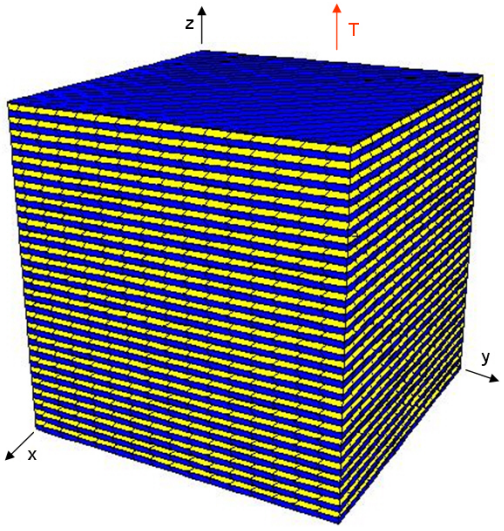

Figure 4.10. *Visualization of [001] simulation subgrain microstructure*

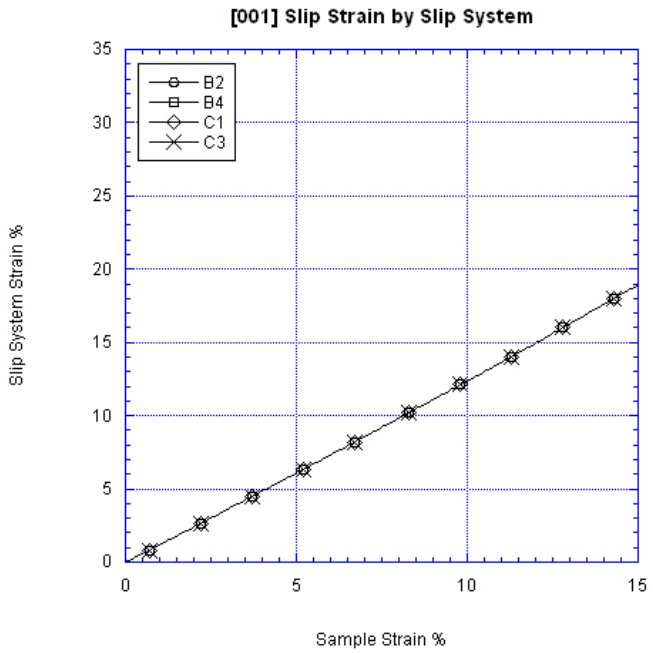

Figure 4.11. *Slip strain on active slip systems for [001] simulation*

available, whether all eight slip systems were activated could be determined by the final shape of the sample. If the final deformed shape is axisymmetric, then all eight slip systems were likely activated as predicted by the Schmidt factor; but if it forms an asymmetric shape, then likely only two slip planes (with four slip systems) activated.

It should also be stated that the rotation of the [001] sample about the 3 axis is substantially influenced by the boundary conditions. To activate the minimum energy deformation patterns displayed, it was necessary to run the sample with the [100] crystal direction parallel to the the [110] sample direction. This is evidence again of the importance of boundary conditions. The small sample size for the [001] simulation may be caused by unknown boundary conditions in the experiments which are not being matched. As the experimental clamping mechanism and the exact orientation of the [001] sample used are unknown, this is impossible to investigate without further experiments.

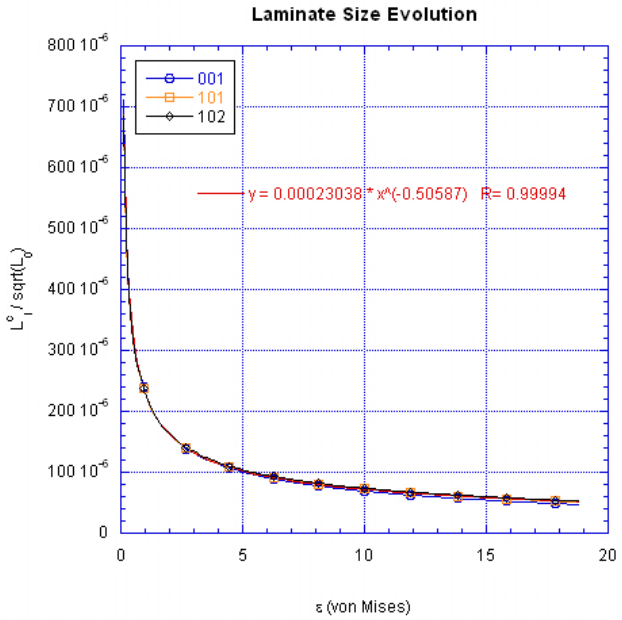

Figure 4.12. *Evolution of laminate thickness scaled by the square root of grain size, $\sqrt{L_0}$, against von Mises strain for the three copper simulations: [101], [102], and [001]*

Figure 4.12 is a plot of the change in the laminate thickness with deformation. It is scaled by the square root of the grain size to remove the effects of grain size on laminate size (cf. equation (3.54)). Note it confirms that the laminates refine with increased slip strain causing parabolic hardening. With the effects of grain size removed, all laminates of all orientations evolve uniformly with increasing strain. The end result can be fit by $\frac{L^c}{\sqrt{L_0}} = 0.00023\epsilon_{vM}^{-\frac{1}{2}}$, as seen in the figure. This relationship can be derived directly from the equation for L_l^c (equation (3.54)) and assuming $W_l^{BL} \approx \frac{1}{2}\mu\delta_l^2$ where μ is the shear modulus. Note that δ is a measure of the plastic strain and since the children do not exist, their boundary layer energy is zero. This yields the approximation that $\frac{L^c}{\sqrt{L_0}} \propto \delta^{-\frac{1}{2}}$.

Hughes et al. [5] measured in aluminum that the average distance between incidental dislocation boundaries (IDB) increases as $\epsilon_{vM}^{-\frac{1}{2}}$ and the average distance between geometrically necessary boundaries (GNB) increases as $\epsilon_{vM}^{-\frac{2}{3}}$. Generally, the laminate model fits

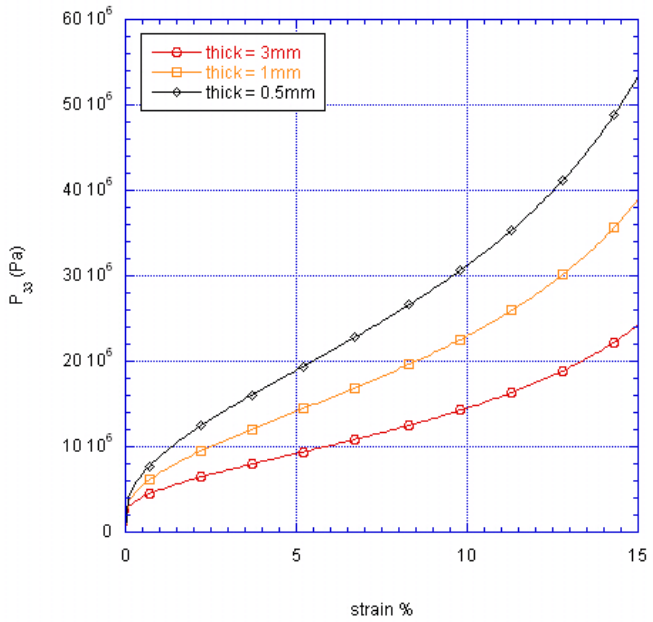

Figure 4.13. *Grain size variation for [102] direction copper single crystals*

GNBs. The difference may be due to uncertainties in the boundary layer energy formulation. Changing the form of the boundary layer energy (equation (3.50)) would produce a different exponent. This is an area that requires further work.

The von Mises strain measure was used in this section as it was used by Hughes et al. for cold rolled samples. The conversion is

$$\epsilon_{vM} = -\frac{2}{\sqrt{3}} \ln(2 - F_{33}) \quad . \tag{4.8}$$

4.3 Grain Size Effects

Figure 4.13 displays the effect of varying the initial grain size using the [102] orientation. The stress increases at a given strain as the initial grain size decreases.

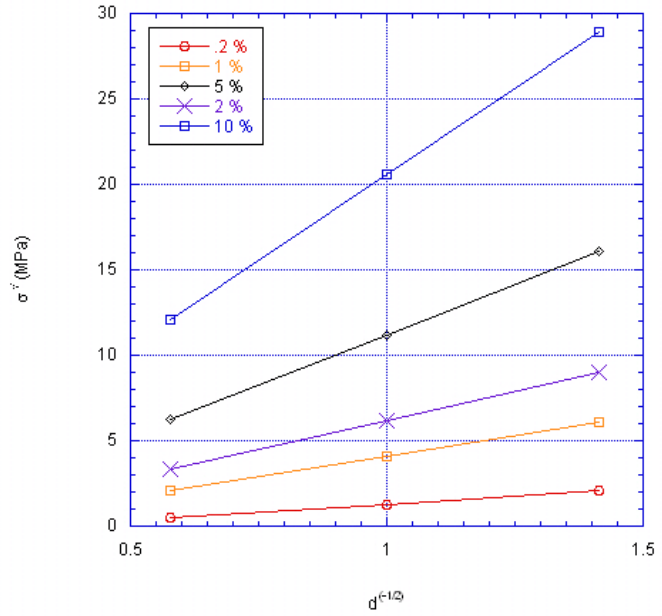

Figure 4.14. *Graph of yield strength at various off-strains vs.* $\frac{1}{\sqrt{L_o}}$ *for the [102] oriented copper single crystal displaying the Hall-Petch effect.*

The increase in critical resolved shear stress due to the formation of dislocation walls varies inversely with the square root of the grain size (i.e., $\Delta\tau_l^c \propto \frac{1}{\sqrt{L_0}}$). This is seen by substituting the laminate length, equation (3.25), into the equation for the mean free path, equation (3.45), and then considering equation (3.46). This promises the Hall-Petch effect [31, 32]: $\sigma^y = \sigma_o + \frac{K}{d^{0.5}}$ where σ^y is yield stress, d is initial grain size, and σ_o is the initial yield stress parameter. The Hall-Petch Effect may be checked directly on the single crystal simulations. This work develops the Hall-Petch effect by modeling of dislocation cell walls. For a review of how a developing dislocation structure yields a Hall-Petch effects see Hansen [33].

Figure 4.14 shows the yield strength of the [102] crystal response against the inverse square root of the initial grain size computed at various offset strains to the linear elastic

deformation. The Hall-Petch relationship holds as the plots are linear. This relationship should hold as long as a single layer of laminate forms, as the case was in all experiments run here. It should also hold for higher-order laminate structures except during the time steps in which the new laminates form.

Uchic et al. [34] and Greer et al. [35] have recent work on the deformation response of micron sized columns of single crystals. This work displayed that single crystals exhibit a Hall-Petch relationship, despite Hall-Petch having been found for polycrystals. The theory presented here shows the Hall-Petch effect due to the formation of dislocation subgrain structure with a grain size dependency, hence it provides an explanation for the Hall-Petch effect for both single crystals and polycrystals. Both Uchic et al. [34] and Greer et al. [35] also predicted a transition as sample size decreased to a "breakaway flow" behavior. This theory would predict that transition as the length scale at which the deformation process no longer favors the formation of dislocation structures, but instead activation of a single slip system. The Uchic et al. experimental data is on a Ni_3Al-Ta alloy and the Greer et al. data is on gold, so no direct comparison is possible. The theory presented here would follow the same trends discovered on the length scale of micron-sized single crystals.

4.4 Grain Shape Effects

All simulations to this point have assumed spherical grains. The grain shape will also affect the deformation response as it changes the ratio of boundary layer to total volume and the initial length parameter will depend on the wall normal of the first laminate formed. The effect of grain shape is explored by assuming three different grain shapes; all with the [101] crystal axis aligned to the tensile axis. The grain shapes simulated are one sphere and two ellipses with one axis, a, twice that of the other two axes. One ellipse has the longer axis

aligned to the [101] crystal axis (and thus aligned to the tensile axis); the other has the longer axis aligned to the [010] crystal direction (perpendicular to the tensile axis). To get an accurate comparison, the elliptical grains' volumes are set equal to the spherical grain volume. This yields $a = \sqrt[3]{4}L_o$ where L_o is the diameter of the spherical grain. The simulated spherical grain has a diameter of 3 mm, yielding $a = 4.76$ mm for the elliptical grains. Due to increased surface area the elliptical grains have 5% more boundary layer volume. This condition is arrived at by taking $\Upsilon = 0.5$ and assuming $L^c \ll L_o$, then comparing surface area volume of a sphere and equal area ellipse with one axis twice the other axes. The boundary layer increase is modeled by setting the parameter Υ to 0.525 for the elliptical grain simulations.

It was assumed each grain forms the same laminate substructure as was seen for the initial spherical [101] simulation (cf. figure 4.3). Since the elliptical grain aligned to the [101] tensile axis forms with dislocation wall normals parallel to the longer ellipse axis, a, it has an initial length of a in which to form laminates. The elliptical grain aligned to the [010] direction for the same reasons has an initial length of $a/2$. Thus, the elliptical grain aligned to the [010] axis has a higher stress than a spherical grain, and the [101] elliptical grain has a lower stress than a spherical grain.

The results of these simulations are shown in figure 4.15. As this grain shape effect is due to the formation of subgrain structures inside the single crystal rather than compatibility constraints within a polycrystalline sample, comparison would need to be made to similar-shaped single crystal tests. As of yet, no information is apparent for comparisons.

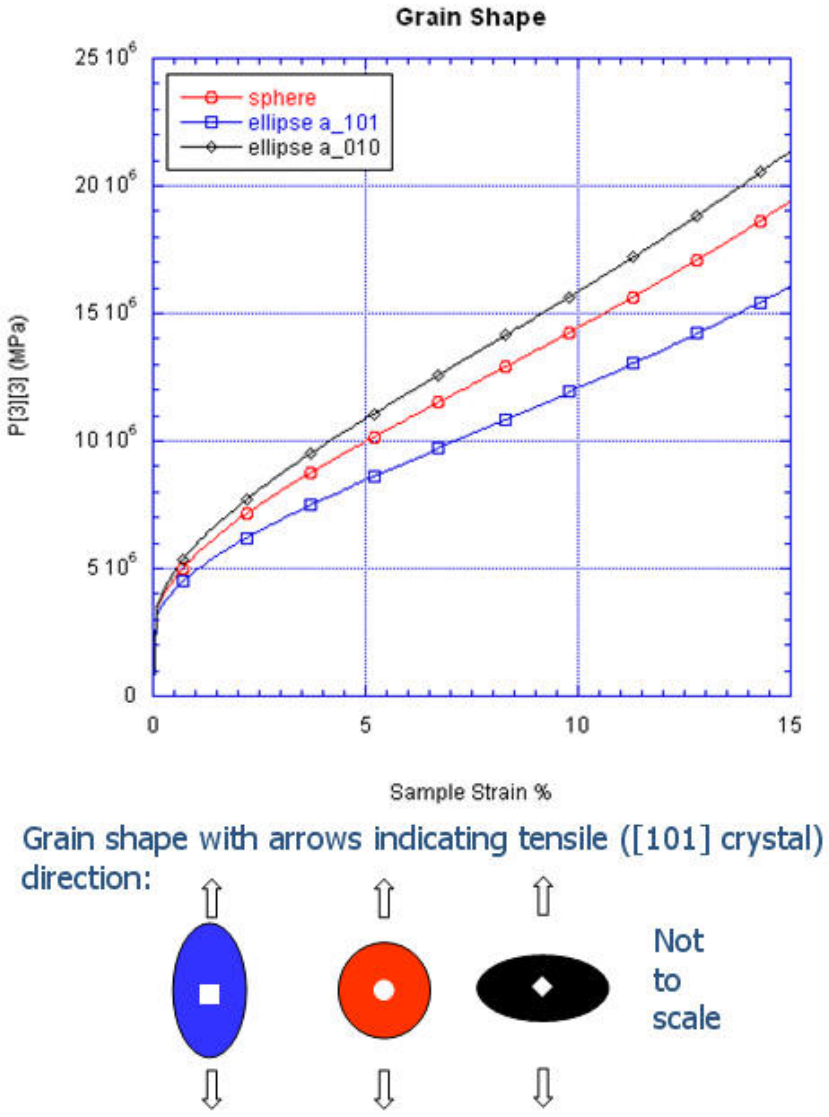

Figure 4.15. *Grain shape effects showing two ellipsoidal grains and one spherical grain for the [101] crystal axis*

Chapter 5

Conclusions and Future Work

A reconfiguration of the laminate model for subgrain dislocation structures has been presented. The model has been modified to include calculation of the mean free path of dislocations incorporating the geometry of the slip plane and the dislocation walls, evolution of the subgrain dislocation laminate length scale over time to capture plastic slip plane hardening, an adjusted boundary layer energy and wall normal implementation, direct minimization of the nonlocal energy terms, and resilience to discontinuities in the stress and material tangent. A method for treating the unique case of coplanar slip laminate structures as a single slip system was also developed to get an appropriate hardening behavior for single crystals.

Addition of dislocation mean free path adjusted for the angle of the slip plane within the microstructure provides for a first approximation of shape effects from interactions within the subgrain laminate structure. The inclusion of dislocation mean free paths calculations drastically affects the selection of activated slip systems and the hardening behavior of slip systems.

Evolution of the width between dislocation wall subgrain structures provides hardening mechanisms akin to those of self and latent hardening. The dimensions of the subgrain structure are determined by minimizing the nonlocal energy. The widths are equilibrated at each deformation step. Self hardening occurs as the laminate width decreases due to in-

creasing boundary layer energy of the laminate microstructure with increased deformation. The crystal bifurcating into separate regions to accommodate activation of new slip systems causes latent hardening to occur. The hardening behavior was validated against experimental tests of single crystal copper. The Hall-Petch effect is returned by the formation of the dislocation subgrain structure. Grain shape effects due to the subgrain structure formation were shown.

The model contains only seven material parameters. All material parameters were measured directly by independent experimentation. It is remarkable that the stress strain response can be predicted so well by the model with no fitting parameters.

Future work also needs to consider the evolution of the volume fraction of laminates, λ_l, to capture the behavior of non-symmetric systems. When structures appear with $\lambda \neq \frac{1}{2}$, it generally means a slip system was activated at a later time during the deformation. This less active slip system then forms with a very small volume fraction, but would increase at each new deformation step. This implies that the volume fraction of the newly formed system would need to increase. If λ_l is not evolved, then the structure has no way of increasing the volume fraction of the system other than continuing to laminate. As this lamination always involves a decrease in the length scale by an order of magnitude, the material will harden too quickly.

The model should exhibit deformation path dependencies due to the formation of dislocation substructure. The path dependency may make it possible to reproduce the stress response to non-monotonic deformation paths. Before these could be implemented the requirement of irreversible plastic slip would need to be relaxed. Rather than using 24 irreversible slip systems, the model needs to be educated with the ability to reverse slip on the

highest rank laminate. Another possibility is to explicitly inform the material model when the deformation path changes occur and allow for slip to change direction.

Further work should consider single crystal experiments that attempt to determine the active slip systems within the microstructure. Further experimental information regarding explicit single crystal size, deformation path, orientation, and microstructure would be useful. Care should be taken to obtain precise boundary conditions as single crystals in uniaxial stress generally do not plastically deform without significant shear strains developing. This would provide further evidence for comparisons between the traditional single crystal plasticity models and this model of subgrain microstructure formation.

Another interesting approach that may be considered for future work is to explicitly map the microstructures that form. Since the microstructure calculations are done in the crystal reference frame, the only inputs to the microstructure model are the material properties, the initial grain length scale, and the deformation gradient. It may be possible to scale the deformation gradient with respect to the material parameters and eliminate those as inputs. If cubic crystals are assumed, it is also possible to place symmetries on the deformation gradient and reduce the space further. The magnitude of the deformation gradient can also be limited for the calculations, as a small discrete time step could be assumed as the maximum $\mathbf{F}$ input to microstructures. This tabulation would provide data for look up as opposed to computing all possible microstructure parameters (i.e., $\lambda_l, N_l, a_l, L_l^c$) at each deformation step. These calculations would not only provide a table for fast future calculations, but would also be interesting in themselves for the map of low energy microstructures.

Bibliography

[1] S Conti and M Ortiz. Dislocation microstructures and the effective behavior of single crystals. *Arch. Rational Mech. Anal.*, pages 103–147, 2005.

[2] P Franciosi and A Zaoui. Multislip in f.c.c. crystals a theoretical approach compared with experimental data. *Acta Metall.*, 30:1627–1637, 1982.

[3] Ellen Cerreta, Los Alamos National Laboratory. Private communication, 2008.

[4] DA Hughes and N Hansen. High angle boundaries formed by grain subdivision mechanisms. *Acta Mater.*, 45:3871–3886, 1997.

[5] DA Hughes, Q Liu, DC Chrzan, and N Hansen. Scaling of microstructural parameters misorientations of deformation induced boundaries. *Acta Mater.*, 45:105–112, 1997.

[6] N Hansen, X Huang, and DA Hughes. Microstructural evolution and hardening parameters. *Materials Science and Engineering*, A317:3–11, 2001.

[7] M Ortiz and EA Repetto. Nonconvex energy minimization and dislocation structures in ductile single crystals. *Journal of the Mechanics and Physics of Solids*, 47:397–462, 1999.

[8] JW Steeds. Dislocation arrangement in copper single crystals as a function of strain. *Proc. R. Soc. Lond. A*, 292:343–373, 1966.

[9] M Oritz, EA Repetto, and L Stainier. A theory of subgrain dislocation structures. *Journal of the Mechanics and Physics of Solids*, 48:2077–2114, 2000.

[10] S Aubrey and M Ortiz. The mechanics of deformation-induced subgrain-dislocation structures in metallic crystals at large strains. *Proc. R. Soc. Lond. A*, 459:3131–3158, 2003.

[11] S Aubrey, M Fago, and M Ortiz. A constrained sequential-lamination algorithm for the simulation of sub-grid microstructure in martensitic materials. *Comput. Methods Appl. Mech. Engrg.*, 192:2823–2843, 2003.

[12] S Conti, P Hauret, and M Ortiz. Concurrent multiscale computing of deformation microstructure by relaxation and local enrichment with application to single-crystal plasticity. *Multiscale Model. Simul.*, 6:135–157, 2007.

[13] E Gurses and M Ortiz. Unpublished manuscript, 2009.

[14] S Conti and F Theil. Single-slip elastoplastic microstructures. *Arch. Rational Mech. Anal.*, 178:125–148, 2005.

[15] AM Cuitino and M Ortiz. Computational modeling of single crystals. *Modeling Simul. Mater. Sci. Eng.*, 1:225–263, 1992.

[16] CA Bronkhorst, BL Hansen, EK Cerreta, and JF Bingert. Modeling the microstructural evolution of metallic polycrystalline materials under localization conditions. *Journal of the Mechanics and Physics of Solids*, 55:2351–2383, 2007.

[17] M Oritz and L Stainier. The variational formulation of viscoplastic constitutive updates. *Comput. Methods Appl. Mech. Engrg.*, 171:419–444, 1999.

[18] JR Rice. *Constitutive Equations in Plasticity Ed. A: Continuum mechanics and thermodynamics of plasticity in relation to microscale deformation mechanisms.* Cambridge, MA: M.I.T. Press, 1975.

[19] EH Lee. Elastic-plastic deformation at finite strains. *J. Appl. Mech.*, 36:1–6, 1969.

[20] C Teodosiu. *Elastic Models of Crystal Defects.* Berlin: Springer, 1982.

[21] JR Rice. Inelastic constitutive relations for solids: an internal-variable theory and its applications to metal plasticity. *J. Mech. Phys. Solids*, 19:433–455, 1971.

[22] RT Rockafellar. *Convex Analysis.* Princeton, NJ: Princeton University Press, 1970.

[23] CA Bronkhorst. *PhD Dissertation: Plastic deformation and crystallographic texture evolution in face-centered cubic materials.* PhD thesis, Massachusetts Institute of Technology, 1991. Appendix F.

[24] KS Havner. On lattice material-frame rotations and crystal hardening in high-symmetry axial loading. *Philosophical Magazine*, 85:2861–2894, 2005.

[25] R Kohn. The relaxation of a double-well energy. *Continuum Mech. Thermodyn.*, 3:193–236, 1991.

[26] P Franciosi. The concepts of latent hardening and strain hardening in metallic single crystals. *Acta Metall.*, 33(9):1601–1612, 1985.

[27] G Simmons and H Wang. *Single crystal elastic constants and calculated aggregate properties: a handbook.* Cambridge, Mass, M.I.T. Press, 1971.

[28] CS Barrett. *Structure of Metals.* New York: McGraw-Hill, 1952.

[29] UF Kocks, AS Argon, and MF Ashby. *Progress in Materials Science: Thermodynamics and Kinetics of Slip.* New York: Pergamon Press, 1975.

[30] SR Kalidindi and L Anand. Large deformation simple compression of a copper single crystal. *Metallurgical Transactions A*, 24A:989–992, 1993.

[31] EO Hall. *Proc. Phys. Soc. B*, 64:747–753, 1951.

[32] NJ Petch. *Journal Iron and Steel Institute*, pages 25–28, 1953.

[33] N Hansen. Hall-petch relation and boundary strengthening. *Scripta Materialia*, 51:801–806, 2004.

[34] MD Uchic, DM Dimiduk, JN Florando, and WD Nix. Sample dimensions influence strength and crystal plasticity. *Scripta Materialia*, 51:801–806, 2004.

[35] JR Greer, WC Oliver, and WD Nix. Size dependence of mechanical properties of gold at the micron scale in the absence of strain gradients. *Acta Materiallia*, 53:1821–1830, 2005.